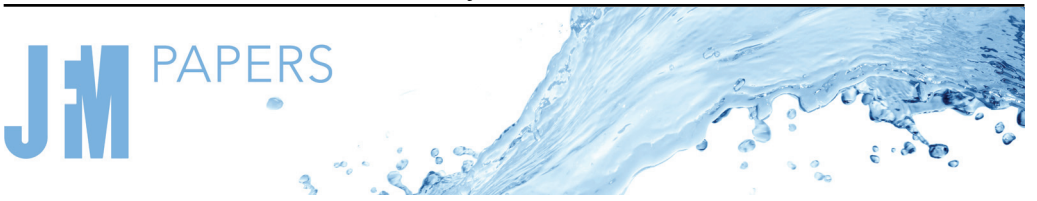
J. Fluid Mech. (2026), *vol.* 1035, A38, doi:10.1017/jfm.2026.11559



Wave-like spirals and spontaneous oscillations in strato-rotational flows

Gabriel Meletti[1], **Stéphane Abide**[2], **Stephane Viazzo**[3], **Jezabel Curbelo**[1,4] **and Uwe Harlander**[5]

[1]Departament de Matemàtiques, Universitat Politècnica de Catalunya - BarcelonaTech (UPC), Av. Diagonal, 647, 08028 Barcelona, Spain

[2]Département de Mathématiques, Université Côte d'Azur, CNRS, Inria, LJAD, France

[3]Laboratoire de Mécanique, Modélisation et Procédés Propre, Aix-Marseille University, CNRS, 38, rue Frederic Joliot Curie, 13451 Marseille, France

[4]Centre de Recerca Matemàtica, Campus de Bellaterra, Edifici C, 08193 Bellaterra, Barcelona, Spain

[5]Department of Aerodynamics and Fluid Mechanics, Brandenburg University of Technology (BTU) Cottbus-Senftenberg, Siemens-Halske-Ring 15a, 03046 Cottbus, Germany

Corresponding authors: Gabriel Meletti, gabriel.meletti@upc.edu; Uwe Harlander, uwe.harlander@b-tu.de

(Received 25 July 2025; revised 11 April 2026; accepted 15 April 2026)

This study investigates the dynamics of strato-rotational instability (SRI) in a stratified, rotating fluid, focusing on the interaction between axial modes and spiral components. Through numerical analysis, we find that SRI induces oscillatory behaviours that change the mean flow, leading to the selective activation of distinct axial wavenumbers associated with upward and downward propagating spiral modes. These results suggest wave–mean flow interactions. The use of Radon transforms (RTs) allowed us to separate these spiral components, showing that each upward and downward component was individually modulated, but out of phase with each other. Inspired by the RT findings, a simplified toy model was developed to interpret the spiral pattern changes linked to amplitude modulations. The model considers two wave-like spirals propagating in opposite axial directions, linearly interacting. By incorporating out-of-phase individual spiral modulations, the model reproduces the observed spiral pattern transitions, offering a straightforward interpretation of the underlying physical processes. To explore the mechanism of individual spiral modulations, we consider a quasi-biennial oscillation (QBO)-like framework derived from the Navier–Stokes aligns in a rotating frame.

© The Author(s), 2026. Published by Cambridge University Press. This is an Open Access article, distributed under the terms of the Creative Commons Attribution licence (https://creativecommons.org/licenses/by/4.0/), which permits unrestricted re-use, distribution and reproduction, provided the original article is properly cited.

https://doi.org/10.1017/jfm.2026.11559 Published online by Cambridge University Press

These findings contribute to a better understanding of low-frequency SRI dynamics and may offer insights into similar phenomena in geophysical and astrophysical contexts.

Key words: rotating flows, stratified flow, waves in rotating fluids

1. Introduction

The interaction between rotation and stable density stratification is frequently found in geophysical and astrophysical flows, often leading to instabilities that play a crucial role in the development of large-scale circulation patterns observed in nature. In geophysical systems such as the Earth's atmosphere and oceans, stratified rotating flows significantly influence weather and climate patterns. A well-known phenomenon in these systems is the quasi-biennial oscillation (QBO), observed in Earth's equatorial stratosphere. The QBO is characterised by a periodic reversal of zonal winds, driven by the emission and interaction of inertia-gravity waves (IGWs) with the mean flow (Lindzen & Holton 1968; Holton & Lindzen 1972; Plumb & McEwan 1978). Understanding the mechanisms underlying the QBO provides valuable insights into the broader dynamics of rotating stratified flows and highlights the importance of wave–mean flow interactions (Seelig & Harlander 2015).

In astrophysical contexts, the interaction between rotation and stable density stratification can be the key to understanding and modelling the formation and evolution of planetary systems that form from accretion disks, as they facilitate the outward transport of angular momentum, allowing matter to aggregate under gravitational forces (Fromang & Lesur 2019; Lyra & Umurhan 2019). Accretion disks are gas and dust structures that have differential Keplerian (or near-Keplerian) velocity profiles (Visser & Dullemond 2010) that can be approximated as a Taylor–Couette (TC) system, which consists of a fluid confined between two independently rotating concentric cylinders. TC systems then serve as a canonical model for investigating the fundamental behaviours of astrophysical rotating flows (Dubrulle *et al.* 2004). When stable density stratification in the axial direction is introduced to a classic TC system, as schematically shown in figure 1(*a*), a purely hydrodynamic instability known as strato-rotational instability (SRI) can develop (Withjack & Chen 1974; Boubnov, Gledzer & Hopfinger 1995; Le Bars & Le Gal 2007). This instability manifests as non-axisymmetric spiral modes, such as those seen in figure 1(*b*), and has gained attention as a potential mechanism for enhancing angular momentum transport in accretion disks. The SRI can destabilise flow regimes that would otherwise be stable under non-stratified conditions, thereby providing a pathway for angular momentum transfer in accretion disks and similar environments (Yavneh, McWilliams & Molemaker 2001; Dubrulle *et al.* 2004; Shalybkov & Rüdiger 2005).

While the SRI arises in the presence of rotation and density stratification, the underlying mechanisms that lead to its development are not yet fully understood. For example, Molemaker, McWilliams & Yavneh (2001) suggests that the SRI results from the interaction between Coriolis and pressure forces, leading to the superposition of two Kelvin waves that resonate in the boundaries of the system. In contrast, Park (2012) and Wang & Balmforth (2018) argue that the SRI could emerge from the spontaneous radiation of internal waves, which reflect and resonate within the cavity, interacting with critical layers to generate the instability, independently of the presence of a rigid outer boundary (Le Dizès & Riedinger 2010).

Recent studies have shown that the SRI can lead to intriguing spiral pattern changes associated with low-frequency velocity modulations observed both numerically and

https://doi.org/10.1017/jfm.2026.11559 Published online by Cambridge University Press

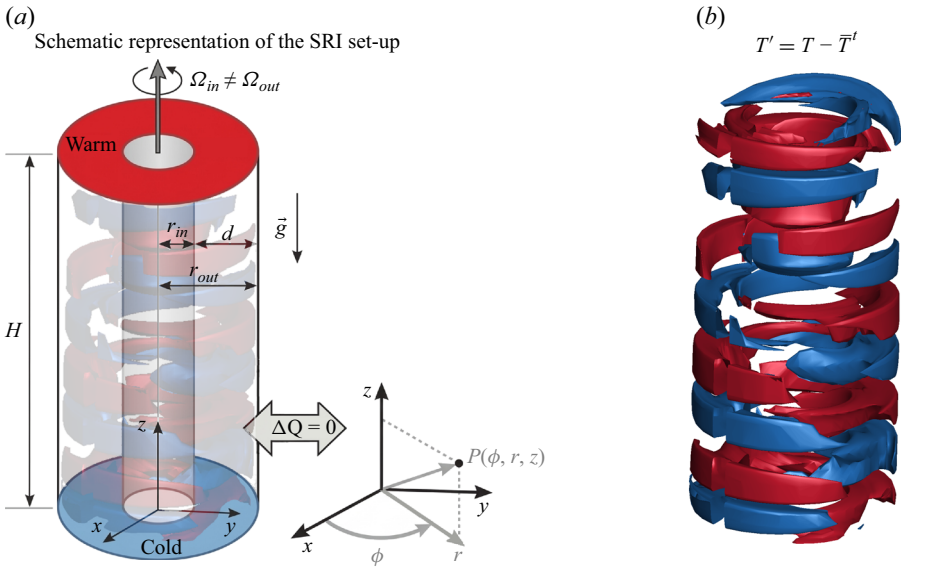


Figure 1. (*a*) Schematic representation of the physical configuration solved numerically in this study, consisting of a Taylor–Couette system filled with an incompressible fluid, with a stable density stratification in the axial direction generated by a thermal gradient. (*b*) Snapshot isocontour of temperature fluctuations $T' = T - \overline{T}^t$ at an arbitrarily chosen time, ranging from -0.07 to $0.07\,^{\circ}\mathrm{C}$.

experimentally (Meletti *et al.* 2020; Lopez & Marques 2022). Meletti *et al.* (2020) linked distinct flow patterns along the axial direction to these modulations. Figure 2, inspired by Meletti *et al.* (2020), shows the patterns associated with amplitude modulations in three distinct time intervals. Each interval displays a unique flow pattern in the space–time diagrams (axial-time frame), which will be further explored in this study. The downward-inclined spiral, presented in figure 2(*b*), travels from the top lid to the bottom in the axial direction, while the upward-inclined spiral, shown in figure 2(*d*), moves in the upward direction. During the transition phase, illustrated in figure 2(*c*) and characterised by a chessboard-like structure and smaller SRI amplitudes (figure 2*a*), the superposition of the two spirals leads to a standing wave pattern. Figure 2(*e–g*) show snapshots of u_z radial–axial ($r-z$) view, at a fixed azimuthal position $\phi = 0$ during three different moments: when the spirals are travelling upwards, downwards and during the transition between these two states, and the SRI spirals do not propagate axially. For better visualisation, illustrative images showing how the SRI manifests as spirals in the stably stratified Taylor–Couette configuration studied here are presented in figure 1, where we show a schematic diagram of the SRI set-up, and a three-dimensional (3-D) visualisation of a temperature fluctuation ($T' = T - \overline{T}^t$) snapshot chosen at an arbitrary time.

The observed SRI spirals share similarities with those found in experiments by Flór *et al.* (2018), where two spirals move in opposite directions, forming a standing pattern, and with simulations presented by Lopez & Marques (2020), with low-frequency modulations due to differences in their axial drift speeds. However, it is important to note that Flór *et al.* (2018) and Lopez & Marques (2020) used a short annulus with a wide gap, where top and bottom boundary effects and centrifugal buoyancy play significant roles. Additionally, unlike the studies by Meletti *et al.* (2020, 2023) and the present paper, Lopez & Marques (2020) employed a smaller Froude number ($Fr < 1$) and a larger Reynolds number ($Re > 6000$). In longer (taller) cavities, spiral pattern changes in the

https://doi.org/10.1017/jfm.2026.11559 Published online by Cambridge University Press

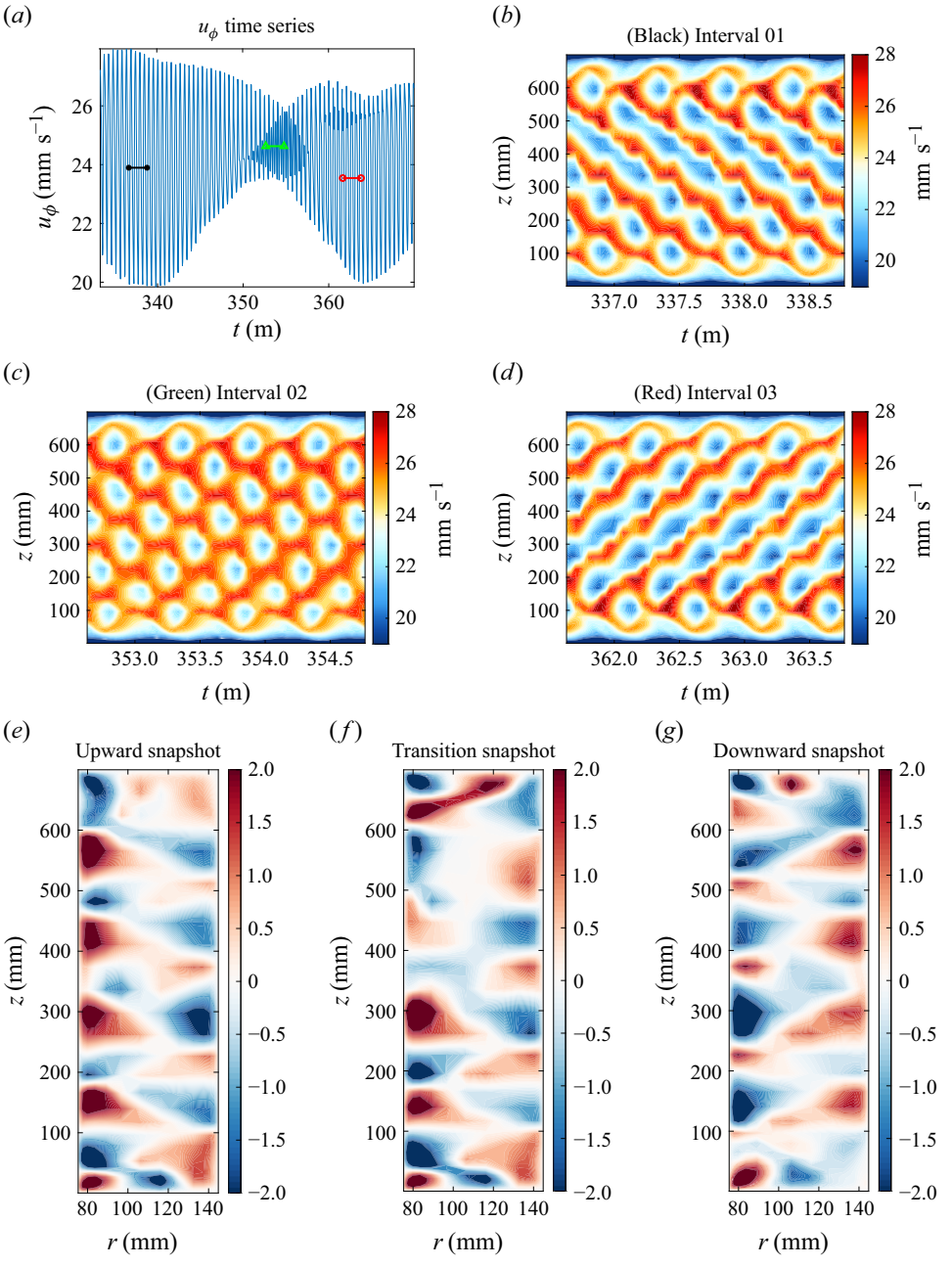


Figure 2. (*a*)–(*d*) u_ϕ structures during amplitude modulation, inspired by Meletti *et al.* (2020): (*a*) time series with horizontal coloured lines indicating intervals selected before (black), during (green) and after (red) the transition; $(r, \phi, z) = (r_{in} + d/2, 0, H/2)$; (*b*) interval 01, from $t \approx$ 336–339 min – SRI spiral with downward inclination; (*c*) interval 02, from $t \approx$ 352–355 min – transition from a SRI spiral with downward to upward inclination; (*d*) interval 03, from $t \approx$ 361–364 min – SRI spiral with upward inclination; $(r, \phi) = (r_{in} + d/3, 0)$. (*e–f*) The radial–axial $(r-z)$ view snapshots of the axial velocity u_z, at a fixed azimuthal position $\phi = 0$ when the spirals are travelling (*e*) upwards; (*f*) during the transition; and (*g*) downwards.

https://doi.org/10.1017/jfm.2026.11559 Published online by Cambridge University Press

axial–radial plane were also observed experimentally by Riedinger, Meunier & Le Dizès (2010).

This present study aims to investigate the mechanisms driving spiral pattern changes in stratified rotating flows. We propose that these spiral pattern changes can be modelled as two individually modulated wave-like spirals, superposed with a phase shift between them. After observing the presence of weak nonlinear features in the modulation of each spiral, we link the mechanism of modulation and pattern changes to QBO-like behaviour.

In § 5, we will apply a WKB approach to qualitatively demonstrate how the waves generated at the boundary due to wave resonance can drive mean flow oscillations in the axial direction. For the WKB method, it is assumed that there is a scale separation in space and time. This means that the variation of the wave's phase is faster than its amplitude, implying that the background conditions vary more slowly than the wave phase. In § 4, we will demonstrate that a toy model with waves showing a slowly varying amplitude and a fast varying phase can successfully reproduce the reversals in the SRI spiral propagation direction. Nevertheless, inspecting figure 2, one could inquire if the validity of the WKB theory has reached its limits since the gap width and the wave's spatial extension are not separated well enough. However, there are examples where, even under such conditions, useful findings were obtained using a WKB approximation. We can consider, for instance, studies of Rossby waveguides in the atmosphere (Hoskins & Ambrizzi 1993) and the oceans (Harlander, Schönfeldt & Metz 2000). For the SRI problem, the WBK approach has also been successfully applied to derive analytical results in previous works such as Yavneh *et al.* (2001), Le Dizès & Billant (2009) and Park & Billant (2013), suggesting that it makes sense to apply this approximation in our context too.

The paper is structured as follows. Section 2 describes the numerical methods used in our study, detailing the direct numerical simulation (DNS) approach, the governing aligns and the boundary conditions. In § 3, we examine variations in the base flow due to the strato-rotational instability (SRI), focusing on the mode activation during spiral pattern changes using two-dimensional fast Fourier transform (2-D-FFT) analysis. We also investigate the behaviour of spiral components by applying the Radon transform (RT) to separate upward and downward travelling spirals. Section 4 introduces a simplified toy model illustrating wave-like spiral propagation to explain the observed pattern transitions. Section 5 proposes a QBO-like model to explain the origin of the amplitude modulations. Finally, § 6 concludes the paper by summarising the key findings.

2. Numerical methods

In this paper, we examine SRI amplitude modulations linked to spiral pattern changes in a Taylor–Couette system subjected to heating from above and cooling from below, which establishes a stable density stratification along the axial (z) direction (i.e. with less dense fluid on top and more dense fluid as we move towards the bottom of the cylindrical cavity along its axial (z)-axis).

We will use the DNS solver developed by Abide *et al.* (2018), considering the same physical model, numerical methods and experimental parameters as we used previously (Seelig, Harlander & Gellert 2018; Meletti *et al.* 2020, 2023), so that the results can be consistent with previous findings. The code employs a fourth-order accurate spatial discretisation and high-performance computing (HPC) (Abide *et al.* 2017, 2018).

The physical model adopts a Taylor–Couette flow configuration filled with an incompressible fluid that is warmed on top and cooled at the bottom, producing a stable density stratification in the axial direction. The physical model is schematically presented in figure 1(*a*).

https://doi.org/10.1017/jfm.2026.11559 Published online by Cambridge University Press

Parameter	Definition	Value
Kinematic viscosity	ν	5.00×10^{-6} m^2 s^{-1}
Thermal diffusivity	$\kappa = k/(\rho c_p)$	8.84×10^{-8} m^2 s^{-1}
Prandtl number	$Pr = \nu/\kappa$	57
Reynolds number (inner cyl.)	$Re = \dfrac{\Omega_{in}\, r_{in}\, d}{\nu}$	400
Inner-cylinder angular speed (implied)	$\Omega_{in} = \dfrac{Re\, \nu}{r_{in}\, d}$	0.381 s^{-1}
Outer-cylinder angular speed (implied)	$\Omega_{out} = 0.35\Omega_{in}$	0.133 s^{-1}
Inner-cylinder rotation period	$T_{in} = 2\pi/\Omega_{in}$	16.5 s
Buoyancy (Brunt–Väisälä) frequency	$N = \sqrt{\alpha g\, \partial_z T}$	0.246 s^{-1}
Froude number	$Fr = \Omega_{in}/N$	1.55
Rossby number	$Ro = \dfrac{u_\phi}{\Omega_{in} d}$	1.07
Ekman number	$E = \dfrac{\nu}{\Omega_{in}\, H^2}$	2.68×10^{-5}

Table 1. Flow parameters and non-dimensional numbers used in this study.

Notes: $r_{in} = 75$ mm, $r_{out} = 145$ mm, $d = r_{out} - r_{in} = 70$ mm, $\eta = r_{in}/r_{out} \approx 0.52$, $H = 700$ mm, $\Gamma = H/d = 10$, $\alpha = 1.08 \times 10^{-3}$ K^{-1}, $\partial_z T = 5.71$ K m^{-1}, $\rho = 923$ kg m^{-3}, $k = 0.133$ W m^{-1}K^{-1}, $c_p = 1630$ J kg^{-1}K^{-1}.

This is the same configuration used to study the SRI experimentally by Meletti *et al.* (2020).

The fluid properties considered are those of the M5 silicon oil used in the experiments presented by Seelig *et al.* (2018) and Meletti *et al.* (2020), with kinematic viscosity $\nu = 5 \times 10^{-6}$ m^2 s^{-1}; specific weight $\rho = 923$ kg m^{-3}; coefficient of thermal expansion $\alpha = 1.08 \times 10^{-3}$ K^{-1}; thermal conductivity $k = 0.133$ W (Km)$^{-1}$; specific heat $c_p = 1630$ J (kg K)$^{-1}$; and Prandtl number $Pr = 57$.

The vertical temperature gradient imposed is of $\Delta T/\Delta z = 5.71$ K m^{-1} and ensures the stable axial density stratification. The geometrical parameters of the TC cylindrical cavity (also presented in the bottom part of table 1) are: inner cylinder radius $r_{in} = 75$ mm, outer cylinder radius $r_{out} = 145$ mm, gap size $d = (r_{out} - r_{in}) = 70$ mm; cylinders height $H = 700$ mm; aspect ratio $\Gamma = 10$; radii ratio $\eta \approx 0.52$.

The numerical code applied here solves the Navier–Stokes aligns using the Boussinesq approximation to incorporate buoyancy forces that, in a rotating frame with angular velocity $\boldsymbol{\Omega}$, and in non-dimensional form, read:

$$\frac{\partial \tilde{\boldsymbol{u}}}{\partial \tilde{t}} + Ro(\tilde{\boldsymbol{u}} \cdot \tilde{\boldsymbol{\nabla}})\tilde{\boldsymbol{u}} + 2\boldsymbol{k} \times \tilde{\boldsymbol{u}} = -\tilde{\boldsymbol{\nabla}}\tilde{p} + \frac{1}{Fr^2 Ro}\tilde{T}\boldsymbol{k} + E\tilde{\boldsymbol{\nabla}}^2\tilde{\boldsymbol{u}}, \tag{2.1}$$

where $\boldsymbol{k} \equiv \boldsymbol{\Omega}/|\boldsymbol{\Omega}|$, $\tilde{\boldsymbol{\nabla}}$ is the non-dimensional gradient operator. Ro is the Rossby number $Ro \equiv U/\Omega L$, $E = \nu/\Omega L^2$ is the Ekman number and $Fr \equiv \Omega/N$ is the Froude number, with N being the buoyancy frequency, here defined as $N = \sqrt{\alpha \boldsymbol{g} \partial T/\partial z}$, where $\boldsymbol{g}$ is the gravity acceleration. In our results, we consider the Reynolds number based on the inner cylinder rotation, as $Re = \Omega_{in} r_{in} d/\nu$. These flow parameters are presented in table 1.

https://doi.org/10.1017/jfm.2026.11559 Published online by Cambridge University Press

For a direct comparison of experimental results (Meletti *et al.* 2020), the Navier–Stokes aligns under the Boussinesq approximation in our code are solved in the dimensional form and in a non-rotating (lab) frame, reading:

$$\begin{cases} \nabla \cdot \boldsymbol{u} = 0 & \text{in } D, \\ \partial_t \boldsymbol{u} + \dfrac{1}{2}\left[(\boldsymbol{u}\cdot\nabla)\boldsymbol{u} + \nabla\cdot(\boldsymbol{u}\boldsymbol{u})\right] = -\nabla p + \nu\Delta\boldsymbol{u} + \boldsymbol{F} & \text{in } D, \\ \partial_t T + \dfrac{1}{2}\left[(\boldsymbol{u}\cdot\nabla)T + \nabla(\boldsymbol{u}T)\right] = \kappa\nabla^2 T & \text{in } D. \end{cases} \tag{2.2}$$

Here, D denotes the computational domain, κ is the fluid's thermal conductivity, p is the pressure, T represents the temperature field, and $\boldsymbol{u} = (u_r, u_\phi, u_z)$ denotes the velocity vector field in the radial, azimuthal and axial directions, respectively. The buoyancy force, denoted by $\boldsymbol{F}$, results from density variations and is defined as

$$\boldsymbol{F} = \alpha \boldsymbol{g} \frac{\partial T}{\partial z} \Delta z. \tag{2.3}$$

All analysis will consider intermediate Reynolds numbers of $Re = 400$, with rotation ratio between inner and outer cylinders $\mu = \Omega_{out}/\Omega_{in} = 0.35$. This value of μ is considered so that we impose a velocity profile that is almost Keplerian (slightly slower), to focus on accretion disk applications (see Visser & Dullemond 2010; Lyra & Umurhan 2019).

In our simulations, velocity boundary conditions are applied at the cylinder walls, with the top and bottom boundaries rotating at the same angular speed as the outer wall. To impose the temperature gradient, the temperature at the top and bottom lids are prescribed as adiabatic Dirichlet boundary conditions. Assuming negligible heat loss through the lateral walls compared with the thermal forcing at the lids, adiabatic boundary conditions are applied laterally, at the inner and outer cylinder's walls. Simulations begin with small, randomly distributed white noise perturbations to trigger instability development. Time discretisation is conducted using the methods proposed by Hugues & Randriamampianina (1998). Spatial discretisation is enhanced using spectral Fourier methods in the azimuthal direction and a fourth-order compact finite difference scheme in the radial and axial directions, as described by Abide & Viazzo (2005). High-performance computing techniques, as detailed by Abide, Binous & Zeghmati (2017), facilitate significant reductions in simulation time through parallelisation. Following Lopez & Marques (2020) and Lopez & Marques (2022), centrifugal buoyancy effects did not present a strong influence in our simulations once the instability was already established and they were therefore omitted from the numerical model. The simulations employ a grid resolution of $32 \times 64 \times 200$ in the $\phi \times r \times z$ directions.

3. Axial modes activation and spiral components separation

In this section, we will present the interaction of the SRI with the base flow and how this is related to the spiral pattern changes. We will further discuss how this is connected to the activation of different axial wavenumbers. Moreover, we discuss how the oscillating behaviour of the spiral axial propagation can be separated into two components, each of them related to weak nonlinear features.

The initial detailed comparison of experimental and numerical data by Meletti *et al.* (2020) identified low-frequency amplitude modulations, as those shown here in figure 2. Similar patterns were later obtained numerically by Lopez & Marques (2022) for a short

https://doi.org/10.1017/jfm.2026.11559 Published online by Cambridge University Press

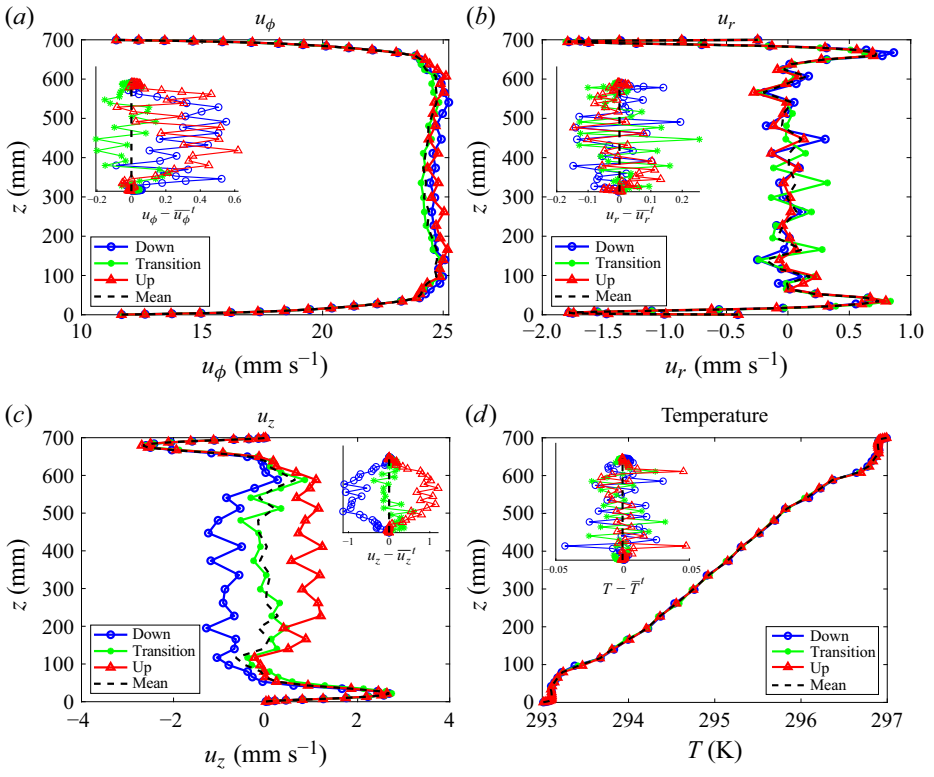


Figure 3. Comparison of the time average axial velocity profiles with time averages taken during an upward travelling spiral period, during a downward travelling spiral period and during the transition from an upward to a downward spiral period. The black dashed line shows the time average over four full periods of amplitude modulations, revealing upward, downward and standing spiral patterns. The results are from numerical simulation performed with $Re = 400$, $\mu = 0.35$ and $\Delta T/\Delta z = 5.7$ K m^{-1} at a fixed radial position $r = r_{in} + d/3$ and $\phi = 0$. The inset in each image shows values of $f - \overline{f}^t$, i.e. the mean values during the upward, downward and transition spiral travelling regime minus the average during the full simulation period.

cylinder geometry. These amplitude modulations occur across all velocity components (u_ϕ, u_r and u_z) and the temperature T, affecting thus the temporal variations of the circulation and the stratification.

Figure 3 shows the time-averaged velocity profiles in the axial direction at a fixed radial position $r = r_{in} + d/2$. The inset in each figure shows $u - \overline{u}^t$, i.e. the velocity minus the total mean value (which is represented by the black dashed line). The time-averaged azimuthal velocity ($\overline{u_\phi}$), displayed in figure 3(a), shows that during the upward or downwards travelling regime (when the velocity amplitude of is larger), the azimuthal flow is slightly accelerated with respect to the mean values or compared with the u_ϕ during the spiral transition between these two regimes. The radial velocity profiles ($\overline{u_r}$) presented in figure 3(b), instead, do not change significantly during the periods when the spirals travel either upwards or downwards, showing no great differences from the overall time average. However, figure 3(c) illustrates how the time-averaged axial velocity ($\overline{u_z}$) is affected by the instability. The mean axial flow becomes positive during upward spiral propagation and negative during downward spiral propagation. During the transition between the two propagation patterns, the average axial velocity approaches zero. These variations in the time-averaged axial velocity are important because they show that

https://doi.org/10.1017/jfm.2026.11559 Published online by Cambridge University Press

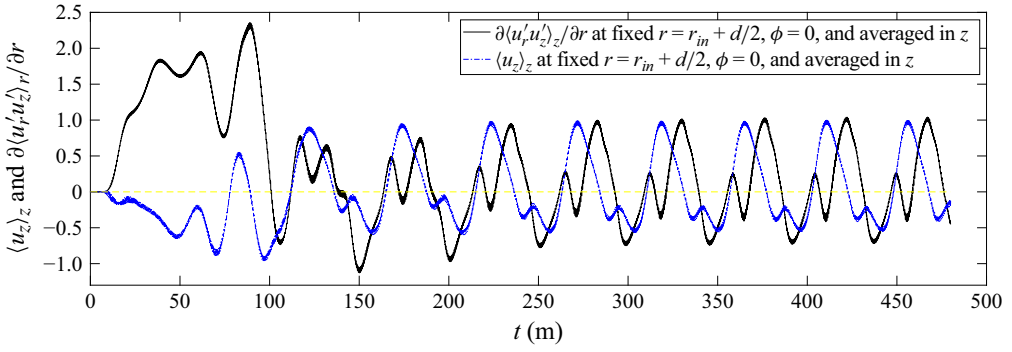


Figure 4. Time series of the wave momentum flux divergence $\partial_r(\langle u_r'u_z'\rangle_z)$ and the axial mean flow $\langle u_z\rangle_z$. The values are averaged in the axial direction and taken at a fixed radial position $r = r_{in} + d/2$ and $\phi = 0$. For wave–mean flow interactions, the momentum flux divergence is the forcing of the mean axial flow. The amplitude of both time series was normalised by the maximum amplitude in the established low-frequency region (for $t > 100$ min).

the spiral propagation affects the mean flow. This connection highlights the interaction between the base flow and the emerging instabilities. Figure 3(*d*) shows the temperature profiles (and their fluctuations). In these cases, we see some difference in temperature fluctuations, of approximately 0.5 °C, especially near the cavity lids, which are considered to be small. Note that near the top and bottom boundaries in figure 3, there is a strong radial inward flow caused by Ekman circulation, with a strong upward flow near the bottom wall and a downward flow near the top wall (shown in the radial velocity presented in figure 3*c*). These Ekman effects are qualitatively similar to those reported by Lopez & Marques (2020). Despite these Ekman effects, simulations with periodic boundary conditions at the top and bottom lids (not presented here) also exhibited amplitude modulations associated with pattern changes (see Meletti *et al.* 2023), showing that the presence of lids and Ekman effects is not the reason for the modulations and pattern transitions to occur.

To better understand the slow axial mean flow oscillations observed in our SRI data, we plot the time series of the eddy momentum flux divergence and the axial mean flow in figure 4. More precisely, at a fixed azimuthal position $\phi = 0$ and at $r = r_{in} + d/2$, we take the axial mean of the momentum flux $u_r'u_z'$ (primes denote the eddy components $u' = u - \overline{u}^t$, i.e. the deviations from the mean) at each time step and compute the derivative of this mean flux with respect to r. In wave–mean flow interaction theory, this eddy flux divergence is the forcing term for the axial mean flow. Clearly, there is a correlation between the axial mean flow and the flux divergence, which suggests that the eddies in the form of the spiral waves force the mean flow oscillations, as will be discussed in more detail in § 5. Note that the time-series were filtered with a 15 min moving average to highlight the low-frequency variations of the mean flow. This time window was chosen arbitrarily. Other periods were also tried for the windowing and the qualitative features observed do not change, considering our purposes here, i.e, using it as a low-pass filter to highlight the low-frequency features.

To investigate if there are changes in the SRI frequency and in the axial wavenumbers during these different spiral propagating regimes, we computed the 2-D-FFT obtained from u_ϕ space–time diagrams in the axial direction (presented in figure 2). Figure 5 shows the results obtained at moments when the spiral is travelling upwards (figure 5*a*, on the left-hand side), downwards (figure 5*c*, on the right-hand side), and during the transition from the upward to the downward propagation (figure 5*b*, middle image). The diagrams in

https://doi.org/10.1017/jfm.2026.11559 Published online by Cambridge University Press

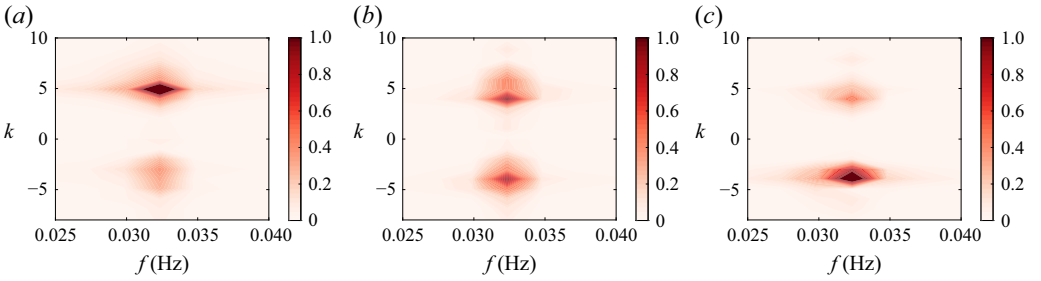


Figure 5. Two-dimensional power spectra of $u_\phi(r)$, computed from the space–time diagrams shown in figure 2(*b–d*) when the spiral is propagating (*a*) upwards; (*b*) during transition from an upward to a downward propagation regime and (*c*) downwards. The x-axis is the frequency in Hz, while the y-axis represents axial wavenumber k (axial modes). The spectra amplitudes are normalised by the maximum amplitude value of the upward (and downward) propagating spirals $P_{0,max}$. The spectra are obtained in a frame of reference fixed in the laboratory. During the transition, the maximum amplitude of the spectra was half of the maximum amplitude found while the spiral was travelling upward or downward ($P/P_{0,max} = 0.5$).

figure 5 present the frequencies f on the x-axis and the axial wavenumber k in the y-axis. We note that the peaks have the same SRI frequencies of $f = 0.032$ Hz independently of the spiral direction of propagation, but they change their wavenumbers from positive to negative values, with different modes being activated and suppressed. During the upward travelling spiral, the stronger wavenumber activated in figure 5(*a*) is $k_{up} = 4$, with maximum amplitude $P_{0,max}$, and the downward mode, which has wavenumber $k_{down} = -4$, is weakly activated. The wavenumber activated with $P_{0,max}$ in figure 5(*c*), related to the downward propagating spiral, is $k_{down} = -4$, while $k_{up} = 4$ has smaller amplitude. In figure 5(*b*), both modes $k_{up} = 4$ and $k_{down} = -4$ are activated, each with approximately half of the maximum amplitude of the spiral travelling upward or downward ($P_{0,max}/2$).

To better understand the spiral oscillatory behaviour and its associated mode activation during the different spiral patterns observed, we separated the up- and downward propagating spirals by applying the RT to the full signal, capturing phases during dominating up, downward and mixed spiral propagation. The RT is a Fourier-like technique to select wave components with different directions of propagation. The RT is particularly suited for finding individual waves that compose noisy or irregular fields (Almar *et al.* 2014). These techniques are interesting for evaluating the results directly using the data obtained, without knowing the wave's dispersion relation and without the necessity of an analytical model of the SRI. A brief description of the RTs can be found in Appendix A.

Figure 6 then shows the separation of the upward and downward components of u_ϕ on a space–time diagram, while the spiral is travelling upward (left-hand side) and downward (right-hand side) using the RT. The results are from the simulation with $Re = 400$, $\mu = 0.35$ and $\Delta T/\Delta z \approx 5.71\ \mathrm{K\ m^{-1}}$ presented in figure 2. After the two wave fields have been separated, we again computed the 2-D-FFT spectra from the corresponding space–time diagrams (not shown here). We observed that the 2-D-FFT of the downward spiral component is exactly the same as the bottom wavenumber in the full 2-D-FFT spectrum presented in figure 5, but the positive frequency is no longer observed (as expected). The upward wavenumber in figure 5 was also captured in the spectrum of the upward component of the upward-travelling spiral (figure 6*e*), but the downward travelling spiral component is removed. Thus, on a simplified model, the wavenumbers we observe in figures 5 can be associated with a superposition of one upward and one

https://doi.org/10.1017/jfm.2026.11559 Published online by Cambridge University Press

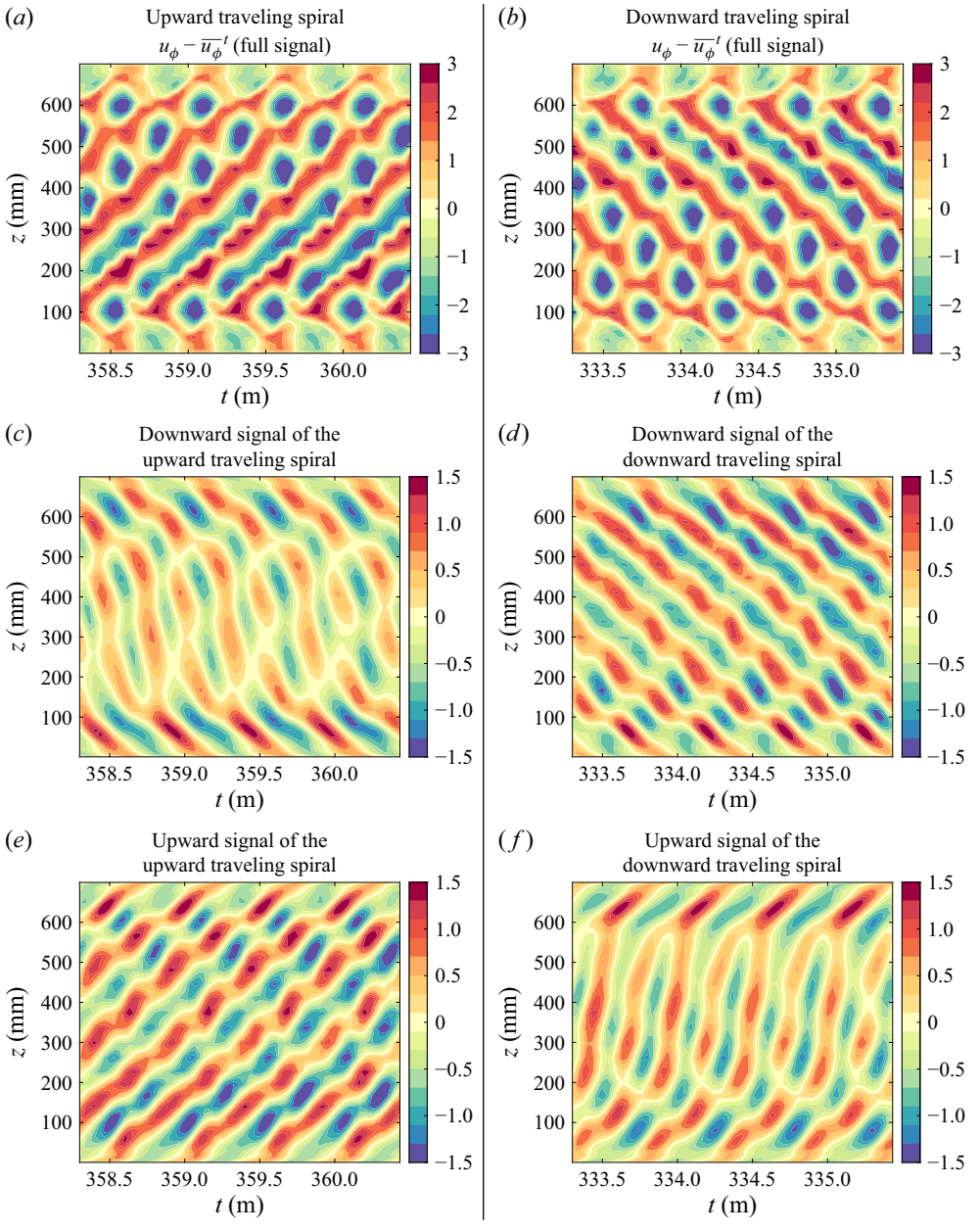


Figure 6. Separation of upward and downward axial travelling components in u_ϕ space–time diagram using the RT. u_ϕ has been taken at $(r, \phi) = (r_{in} + d/2, 0)$. Panels (*a*), (*c*), (*e*) show time intervals when the spiral is travelling upwards. Panels (*b*), (*d*), (*f*) show time intervals when the spiral is travelling downwards. Panels (*a*), (*b*) show the full space–time diagram minus the mean flow (computed using the full time signal). Panels (*c–f*) show the separated upward and downward travelling components obtained using the RT (applied to the full signal, but it filters out the mean flow when it is applied). Simulation performed with $Re = 400$, $\mu = 0.35$, $\Delta T/\Delta z \approx 5.71\text{K m}^{-1}$ and $H = 700\,\text{mm}$.

https://doi.org/10.1017/jfm.2026.11559 Published online by Cambridge University Press

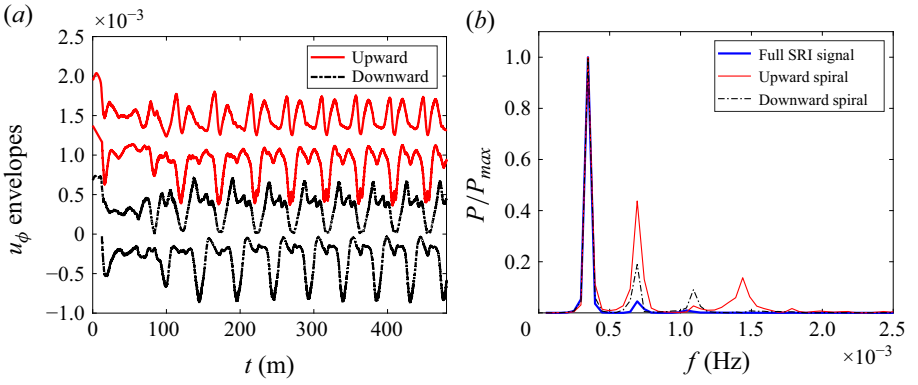


Figure 7. (*a*) u'_ϕ upward and downward spiral components amplitude modulations taken at $(r, \phi, z) = (r_{in} + d/2, 0, H/2)$. The upward travelling time series was arbitrarily dislocated in the vertical axis for better visualisation (originally, both time series were on top of each other). (*b*) Power spectra obtained from the amplitude envelopes of the u_r time series, and of their separated upward and downward components, obtained using the RT to separate the signals. The time series is obtained from numerical simulations with $Re = 400$, $\mu = 0.35$ and $\Delta T/\Delta z \approx 5.71$ K m^{-1}.

downward spiral of axial wavenumber $k = 4$ and $k = -4$ propagating in time with the SRI frequency (see Meletti *et al.* 2020 for more details on the SRI frequency measurements and values). In other words, while the spiral is propagating downwards, we see in figure 6 that the spiral travelling upwards is suppressed, reaching smaller amplitudes and a more vertical inclination (figure 6*f*). The same occurs with the downward component when the spiral is propagating upwards (figure 6*c*). This approach fully confirms the results shown in figure 5, namely that each separated mode is indeed associated with the spiral components travelling upwards and downwards without any changes in the frequency, but with changes in their wavenumbers. This implies that a linear superposition of the two spirals should explain some part of the amplitude modulation. As an extension of the analysis, we also examined the RT on a more complex case involving a taller cavity with $H = 2800$ mm (four times taller than the configuration considered here). In this set-up, the flow exhibits more complicated spiral patterns, but all the conclusions we can obtain from those results are consistent with those presented here, i.e. we observe similar regions being activated/deactivated depending on whether the spiral is moving upwards or downwards in a given time. These additional results are presented in Appendix B.

Figure 7(*a*) shows the time series envelope of separated upward and downward spiral components. Note that this is not the full SRI velocity, which presents faster oscillations (see Meletti *et al.* 2020), but just the envelope capturing the velocity amplitude modulations. The upward travelling time series was arbitrarily dislocated in the vertical axis for better visualisation (originally, both time series were on top of each other). Note that, also here, when the amplitude of the downward spiral is enhanced, the upward spiral amplitude becomes smaller (and *vice versa*), showing a phase shift of the up-downward components beating. When the power spectrum of the u_ϕ amplitude envelope is compared with the separated upward and downward components obtained by using the RT in figure 7(*b*), the same (low) frequencies are observed.

Note that we can observe harmonics in the envelope spectra presented in figure 7(*b*), and also on each of the separated up and downward spiral components, which suggests a weak nonlinear interaction and not simply a linear interaction of two waves travelling with different frequencies. Note also that the amplitudes of each separated spiral component

https://doi.org/10.1017/jfm.2026.11559 Published online by Cambridge University Press

in the power spectra differ from those obtained from the full velocity signal. A similar behaviour is obtained from the u_ϕ, u_r and u_z time series, i.e. with peaks corresponding to the same frequencies in Hz, but with different amplitudes P and P_{max}. However, most importantly, we would like to highlight that, when the Radon filtering is applied, we observe a clear phase shift in the modulations of each separated component when we look at the time series in figure 7(*a*). This phase shift indicates that the harmonics observed in the spectra are not simply modulated in isolation; rather, they suggest a nonlinear interaction, causing the modulations. The fact that these modulations cannot be fully explained by linear interactions alone implies that a more complex dynamic is at play, where the interaction between the spirals and the mean flow results in the alternating strengthening and weakening of the SRI spiral components. This interaction, in turn, leads to the observed alternation between upward and downward propagating modes, each with varying amplitudes. In the following sections, we will investigate how these two individually modulated components could lead to the pattern formations we observed.

4. Toy model: wave-like spiral propagation

In this section, we introduce a toy model consisting of two waves travelling in opposite axial directions to demonstrate how the linear superposition of the SRI spirals can lead to pattern changes. This approach is inspired by the separation of the spirals using the RT technique. We observed in the previous sections that each spiral (travelling upward and downward) is individually modulated and phase-shifted relative to one another. The reasons behind the modulation of each spiral will be discussed later in this paper. For now, we assume that the spirals behave as two individual plane waves, described by the following aligns:

$$\begin{aligned} \text{wave}_1 &= A_1 \cos\left((m_1 x + l_1 y + k_1 z) - \omega t\right), \\ \text{wave}_2 &= A_2 \cos\left((m_2 x + l_2 y + k_2 z) - \omega t\right), \\ u_{toy} &= \text{wave}_1 + \text{wave}_2, \end{aligned} \tag{4.1}$$

with $0 \leqslant x, y, z \leqslant 2\pi$, and amplitudes A_1 and A_2. The values of $0 < x, y, z < 2\pi$ result from normalising the cavity height (e.g. $0\,\text{mm} < z < 700\,\text{mm}$). The amplitude of each plane wave is modulated, and they must be out of phase to achieve the inclined spirals with constructive and destructive interference while they propagate. In the toy model, sinusoidal amplitude modulations A_1 and A_2 are considered out of phase with an angle θ, written as

$$\begin{aligned} A_1 &= A \sin(\omega_A t), \\ A_2 &= A \sin(\omega_A t + \theta), \end{aligned} \tag{4.2}$$

where A is a given real value, and $\omega_A << \omega$ is the amplitude modulation of each wave, here considered to be the same for A_1 and A_2.

Figure 8 shows the space–time diagram obtained with this toy model, with wavenumbers in the azimuthal, radial and axial directions $(m = 1, l = 1, k = 4)$ and $(m = 1, l = 1, k = -4)$, similar to those previously observed in our simulations (with $Re = 400$, $\mu = 0.35$, $\Delta T/\Delta z \approx 5.71\ \text{K m}^{-1}$ and $H = 700\,\text{mm}$). It is possible to see that the linear superposition of both upward and downward waves, each individually modulated and travelling out of phase, could lead to the final spiral pattern transitions observed in the previous sections. The amplitude modulations of the waves presented in figure 8 are out of phase with an angle $\theta = \pi/3$, but other different phase shifts (and different wavenumbers) produce similar pattern changes.

https://doi.org/10.1017/jfm.2026.11559 Published online by Cambridge University Press

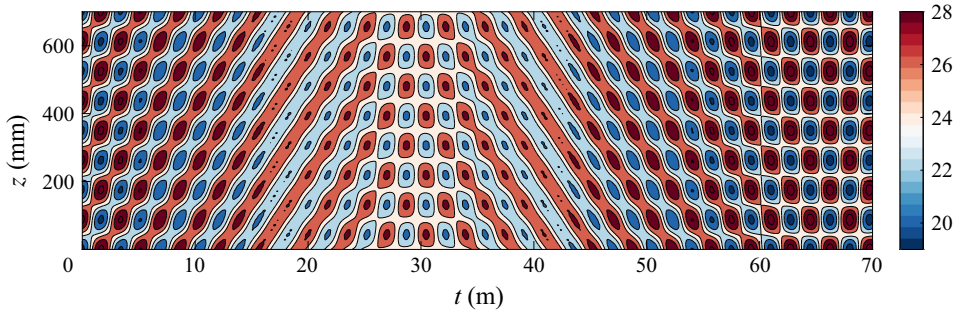


Figure 8. u_{toy} space–time diagram of the toy model composed of two plane waves with sinusoidal amplitude modulations with $\omega_A = 7 \times 10^{-4}$, out of phase by an angle $\theta = \pi/3$, and travelling in opposite axial directions with wavenumbers of wave$_1$ and wave$_2$ respectively $(m_1, l_1, k_1) = (1, 1, 4)$ and $(m_2, l_2, k_2) = (1, 1, -4)$. The frequency $\omega = 0.03$ and the maximum amplitude of each wave is $A = 10$. Data taken at $(x, y) = (0, \pi)$.

The toy model and the numerical simulation also show good qualitative agreement when we compare snapshots, i.e. looking at the space structures at given times while the spirals are travelling upward, downward and during the transition. This comparison can be seen in figure 9, where we can see that the results are similar, except for the fact that the spirals in the simulations are confined in a slightly smaller region, due to Ekman effects. The good qualitative agreement of this simplified toy model with the numerical simulations, as well as the possibility of reproducing the spiral pattern changes previously investigated using similar wavenumbers and frequencies obtained from numerical simulations and experimental measurements, shows that this linear superposition of the spirals can drive the spiral pattern changes. In this case, each up and downward component should be interacting with the mean flow that, at times, provides more energy to the upward travelling spiral, and at other times, provides more energy to the downward component. The reason why each individual spiral is modulated will be interpreted as a QBO-like mechanism in the following section, inspired by the fact that the spiral propagation direction affects the mean flow structure (see figure 3). Therefore, each spiral component must be interacting with the mean flow to achieve its individual (phase-shifted) modulation, so that the linear superposition of these two modulated components will lead to the reversal of the spiral direction as presented here in this toy model.

5. Axial mean flow interpretation considering inertial wave interactions

Based on previous observations of mean flow variations associated with the oscillatory spiral behaviour and given that the toy model introduced in the previous section successfully reproduces these pattern changes, we will now interpret the low-frequency amplitude modulation of the SRI as a QBO-like phenomenon. This interpretation is suggested by figures 3(*c*) and 4, as we will discuss in the following.

We would like to emphasise that employing a QBO-like model to interpret our SRI data is a simplified approach intended to understand the mechanisms responsible for the amplitude modulations we observed. This analogy is motivated by certain dynamical similarities between the SRI and the QBO.

5.1. *Dynamical similarities between the SRI and the QBO, and its limitations*

The analogy between a QBO-like model and the SRI is motivated by certain dynamical similarities that we can observe between them. However, a direct comparison is not

https://doi.org/10.1017/jfm.2026.11559 Published online by Cambridge University Press

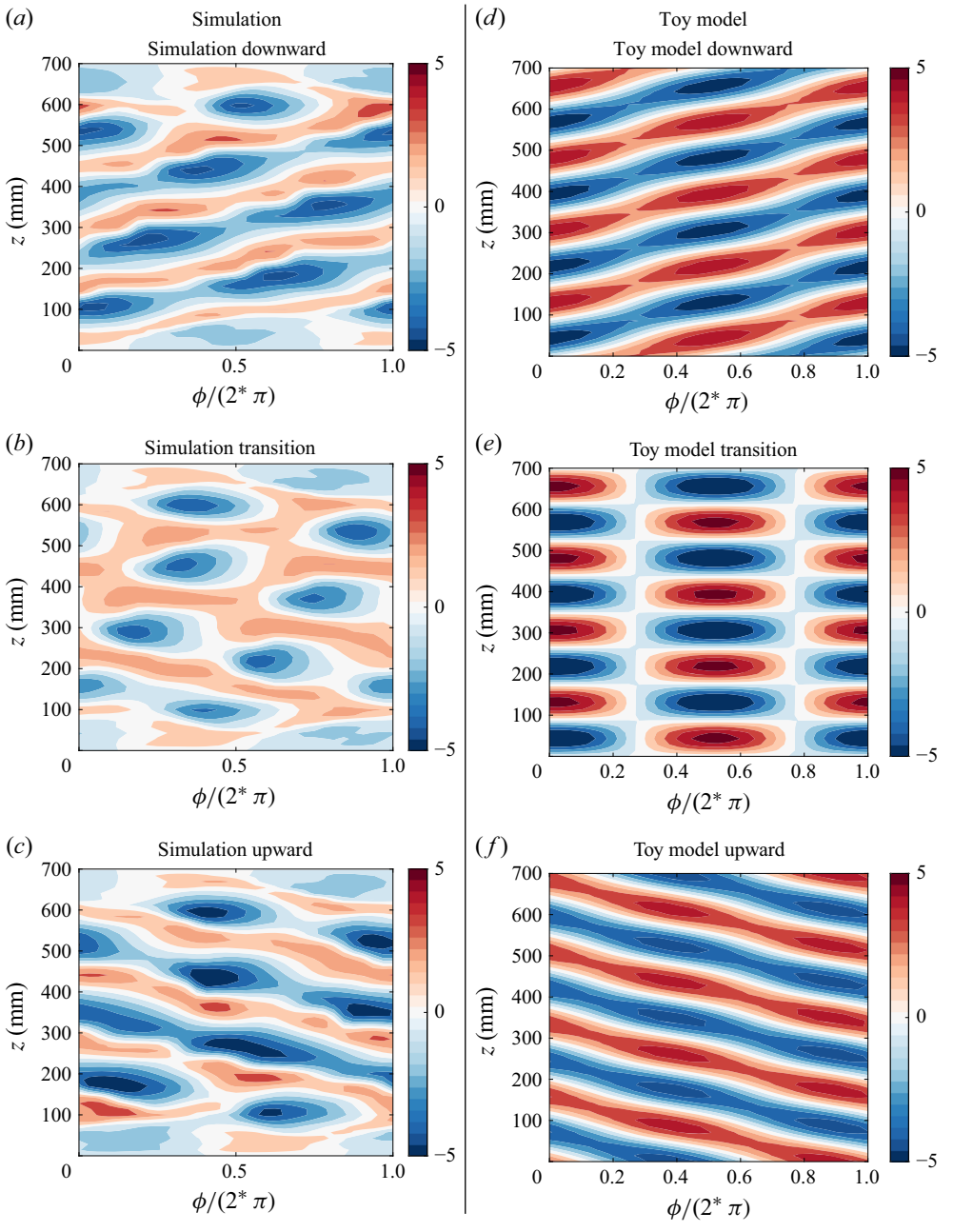


Figure 9. Snapshots with different spiral patterns in the ϕ–z cross-section comparing $u'_\phi = u_\phi - \overline{u_\phi}$ obtained from(a–c) numerical simulations fixed at a radial position $r \approx r_{in} + d/3$ and(d,e,f) the toy model. Panels (a), (d) show moments when the spirals are travelling downwards; panels (b), (e) show the transition; and panels (c), (f) show spirals travelling upwards. The simulations were performed with $Re = 400$, $\mu = 0.35$ and $\Delta T/\Delta z \approx 5.71\ \mathrm{K\ m^{-1}}$. The toy model consists of two plane waves at $y = \pi$ with frequency $\omega = 0.001$, and wavenumbers $(m_1, l_1, k_1) = (1, 1, 4)$ and $(m_2, l_2, k_2) = (1, 1, -4)$, wave amplitude $A = 3\ \mathrm{mm\ s^{-1}}$, and modulation frequency $\omega_A = 0.01$ with $\theta = \pi/2$ phase difference.

https://doi.org/10.1017/jfm.2026.11559 Published online by Cambridge University Press

straightforward if we consider, for example, that the SRI develops in a system that is bounded between the inner and the outer cylinders, differently from the QBO (Holton & Lindzen 1972; Plumb 1977). Therefore, we will consider a QBO-like forcing mechanism at $r = r_{in}$ and $r = r_{out}$ separately, i.e. we model the forcing as two standing waves at each boundary separately (assuming, for simplicity, that oscillations from one source do not interact with those from the other). Moreover, we have to formulate the implicit hypothesis that the QBO-like forcing, and hence the wave momentum in the region near the boundaries, is due to waves generated by the SRI and not, as in standard QBO models, by bottom topography. However, due to wave resonance, the linear instabilities lead to a growth of perturbations at the boundaries similar to the topographic case. This growth is halted primarily due to nonlinear saturation and possibly dissipation. Compared with topographic forcing, this makes it difficult to prescribe the initial amplitude of the wave forcing at the boundaries. Nevertheless, it is useful to point out a few shared features that justify considering this analogy, with some qualitative similarities between the SRI data and the QBO predictions.

(i) For the QBO, a bifurcation occurs from a rest state to an oscillatory state driven by wave forcing. Meletti *et al.* (2023), in a parametric study, showed that the faster SRI oscillations (spirals) can develop in the flow without exhibiting low-frequency amplitude modulations. The development of such modulations is therefore interpreted as a secondary instability that can be triggered (or not) depending on the imposed forcing, analogous to the behaviour observed in the QBO by Holton & Lindzen (1972) and Plumb (1977). Moreover, our results show that the regular, slower amplitude modulation investigated here appears only after the SRI spirals are fully established. The preceding regime, before the modulation becomes periodic, is thus regarded as a transient phase associated with the onset of the secondary instability. In figure 7, we see that the transient regime takes approximately 100 minutes in our case. During this transition, the amplitude of the SRI waves remains smaller than in the modulated regime. These observations suggest that the low-frequency modulations originate from a bifurcation from a steady oscillatory state (characterised by pure SRI spirals) to a modulated oscillatory state, driven by a wave forcing imposed, analogous to the QBO.

(ii) In a QBO-like model, the velocity amplitude should be bounded by the phase speed of the counter-propagating waves (Holton & Lindzen 1972; Plumb 1977). For the highlighted case (see figure 3*c*), we indeed find $|c| > |u_z|$, i.e. the axial mean flow is bounded by the axial phase speed of the spirals with $|c| \approx 4.6$ mm s^{-1} and $|u_z| \approx 1.46$ mm s^{-1}.

(iii) The oscillations of the mean azimuthal flow are accompanied by phase-shifted oscillations in the momentum flux, as shown by Meletti *et al.* (2023), indicating a clear wave–mean flow interaction. This behaviour is consistent with a QBO-like oscillation, where alternating momentum deposition by waves drives periodic reversals of the mean flow. Such coupling between momentum flux and the mean-flow variability (observed here previously) inspires this comparison with the temporal modulation of wave-induced momentum transport with an oscillatory dynamics, similar to the QBO.

(iv) For the QBO, the period of the mean flow oscillations is proportional to the inverse of the amplitude squared. We analysed the simulations with the Reynolds numbers $Re = 300$, $Re = 400$ and $Re = 600$, for which we found low-frequency modulations of the axial flow. We found for $Re = (300, 400, 600)$ that $1/A^2 = \gamma T$ with $\gamma = (16.88, 16.96, 15.22\ \mathrm{s\ m^{-2}})$, indicating that the observed oscillations are

https://doi.org/10.1017/jfm.2026.11559 Published online by Cambridge University Press

due to wave–mean flow interactions. Note that we have taken the data at a radial distance $R/3$ and mid-height, but we verified that the same $T \sim 1/A^2$ scaling also holds at other radial positions. The low-frequency oscillation periods found for $Re = 300$, $Re = 400$ and $Re = 600$ in seconds were respectively $T_{Re=300} = 7334$ s, $T_{Re=400} = 2818$ s and $T_{Re=600} = 1094$ s.

(v) Finally, the velocity amplitude modulations we observe in figure 7(*a*) are linked to the travelling spiral direction (figure 2) in a weakly nonlinear manner, given that we see harmonics in the envelope spectra, indicating an interaction between the base flow and the instability.

Therefore, a simplified QBO model might capture several qualitative features of the SRI dynamics, even if a direct comparison between the two systems is not straightforward. One relevant difference that we mentioned previously comes from the fact that the SRI flow develops in a bounded domain, and the vortices trapped near the inner and outer walls strongly influence the large-scale modulation patterns. When examining the flow dynamics away from the boundaries, however, the SRI data and the QBO-like model exhibit comparable qualitative behaviour, such as the alternating reversals and amplitude modulations of the mean flow we observed.

5.2. *Derivation of the QBO-like aligns applied to the SRI reversals*

To consider these modulations as a QBO-like phenomenon occurring in stratified rotating shear flow, our approach follows the ideas presented by Holton & Lindzen (1972), Plumb (1977), Seelig & Harlander (2015) and Renaud & Venaille (2020), but focuses on inertial waves due to the weak stratification in the SRI simulation. Instead of considering the classical non-rotating but stratified QBO scenario, where the base flow in the azimuthal direction produces a QBO in the azimuthal–radial plane, we consider the base flow in the axial direction generating the QBO in the axial–radial plane. In other words, we will show here how the wave interactions in the axial–radial plane can drive an oscillating axial mean flow. Since, for the flow discussed here, the ratio between the Coriolis parameter $f = 2\Omega_{in}$ and the buoyancy frequency N is larger than 1 ($f/N = 3$), we focus here on inertial waves and not on internal gravity waves as in the model by Holton & Lindzen (1972) and Plumb (1977). However, we will see that the aligns are analogous to aligns for the atmospheric QBO in the equatorial stratosphere, driven by internal gravity waves. The analysis is local Cartesian, as presented in figure 10; that is, we neglect curvature. For further simplification, the diffusion terms in the Plumb (1977) model are replaced by viscous drag terms with a drag coefficient ς. Note that we neglect the azimuthal x-dependency in the inertial wave-based QBO model by assuming that this dependency is weak. Only then can we derive a model that is isomorphic to the classical 2-D QBO model. This is in analogy to the internal gravity wave model of Lindzen & Holton (1968), Holton & Lindzen (1972) and Plumb (1977), for which the meridional dependency had been skipped. Then, the momentum aligns in a frame co-rotating with Ω_{in} read

$$\partial_t u + v\partial_y u + w\partial_z u = -2\Omega_{in} w - \varsigma u, \tag{5.1}$$

$$\partial_t v + v\partial_y v + w\partial_z v = -\frac{1}{\rho_0}\partial_y p - \varsigma v, \tag{5.2}$$

$$\partial_t w + v\partial_y w + w\partial_z w = -\frac{1}{\rho_0}\partial_z p + 2\Omega_{in} u - \varsigma w, \tag{5.3}$$

https://doi.org/10.1017/jfm.2026.11559 Published online by Cambridge University Press

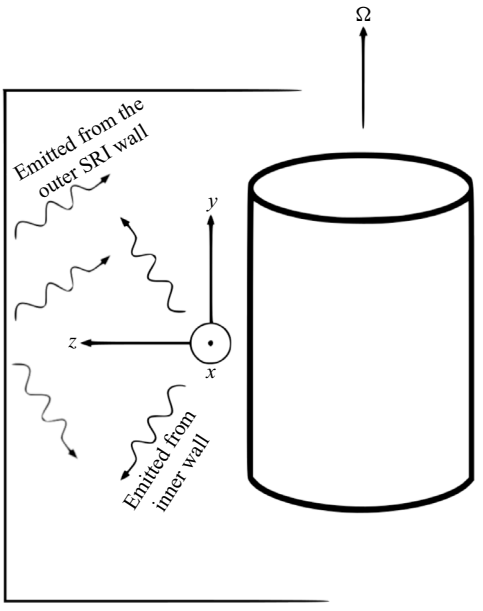


Figure 10. Local Cartesian coordinate system used for (5.1)–(5.3). Waves propagating in the z–y-plane are sketched. Note that in such a 'planetary model', the rotation vector and the gravity vector are perpendicular to each other. In contrast, these vectors would be parallel and in the opposite direction in the SRI-cylinder. In our model, we neglected the explicit gravity term for simplicity.

where (y, z) are the axial and radial directions, respectively, and (u, v, w) are the azimuthal, axial and radial velocity components (see figure 10). Here, p is the generalised pressure that includes centrifugal effects. Note that, in contrast to the strictly 2-D internal wave QBO model, for inertial waves, the flow is 3-D even though all dependent variables depend only on t, y and z.

Defining the streamfunction $\psi = \psi(y, z, t)$ and a zonal momentum $\tilde{u}$ as

$$v = -\partial_z \psi, \quad w = \partial_y \psi, \quad \tilde{u} = 2\Omega_{in} u, \tag{5.4}$$

this system can be reduced to

$$\partial_t \nabla^2 \psi + J(\psi, \nabla^2 \psi) = \partial_y \tilde{u} - \varsigma \nabla^2 \psi, \tag{5.5}$$

$$\partial_t \tilde{u} + J(\psi, \tilde{u}) = -4\Omega_{in}^2 \partial_y \psi - \varsigma \tilde{u}. \tag{5.6}$$

By introducing the streamfunction in the azimuthal–radial plane,

$$\psi = \psi(x, z, t), \quad u = -\partial_z \psi, \quad w = \partial_x \psi, \tag{5.7}$$

and with a gravity vector pointing in the negative z-direction, Holton & Lindzen (1972) and Plumb (1977) derived the following align for the case of internal gravity waves:

$$\partial_t \nabla^2 \psi + J(\psi, \nabla^2 \psi) = \partial_x b + \nu \nabla^4 \psi, \tag{5.8}$$

$$\partial_t b + J(\psi, b) = -N^2 \partial_x \psi - \mu b, \tag{5.9}$$

where $b = -g\rho'/\rho_0$ is buoyancy, ρ' and ρ_0 is the density perturbation and the mean density, ν is the kinematic viscosity, and $N^2 = -(g/\rho_0)\mathrm{d}\bar{\rho}/\mathrm{d}z$ is the square of the buoyancy frequency, where $\bar{\rho}$ is the background density with a linear dependency on z. Here, there is no rotation, and in contrast to the previous case, the waves propagate in the

https://doi.org/10.1017/jfm.2026.11559 Published online by Cambridge University Press

azimuthal–radial plane (the x–z-plane). Except the linear friction term in (5.5), the (5.8), (5.9) and (5.5), (5.6) are mathematically isomorphic. Friction terms are also used, e.g. in simple models for vorticity Ekman pumping (Pedlosky 1987).

To derive a 'QBO model' from (5.5) and (5.6), we can proceed in the same way as for the gravity waves. First, a mean state $\bar{\psi}$ is defined, the streamfunction is written as $\psi(y, z, t) = \bar{\psi}(z) + \epsilon\psi'(y, z, t)$ and the aligns are linearised about the mean streamfunction $\bar{\psi}$, where $\psi'(y, z, t)$ is the fluctuation around the mean value and ϵ is a small perturbation parameter, $\epsilon \ll 1$. The perturbation is expanded as $\psi'(y, z, t) = \phi(z)\exp(il(y - ct))$, where l is the axial wave number and c the axial phase speed. We obtain a linear align for $\phi(z)$, and its solution gives the perturbation velocities v' and w'. Then, assuming periodic boundary conditions in the axial y-direction, (5.2) is averaged over this direction to obtain

$$\partial_t \bar{v} + \varsigma \bar{v} = -\epsilon^2 \partial_z(\overline{v'w'}), \tag{5.10}$$

where $\bar{v} = -\partial_z\bar{\psi}$ is the slowly varying and z-dependent mean flow in the axial y-direction. Note that the forcing term on the right-hand side of (5.10) is analogous to the eddy forcing term we computed for the SRI simulations and plotted in figure 4. Note further that even though the SRI-cylinder is bounded by a top and bottom lid, for deriving (5.10), we considered periodicity in the axial direction. This simplification is motivated by findings of Meletti *et al.* (2023) showing that the slow axial flow modulations also occur under axially periodic boundary conditions. To draw an analogy with Plumb (1977), we will now focus here on the QBO-like phenomenon induced by a single boundary (inner cylinder wall).

5.3. *QBO-like oscillations induced by the inner boundary*

Plumb (1977) found for the atmospheric QBO case,

$$\partial_t \bar{u} - \nu\partial_{zz}\bar{u} = -\epsilon^2 \partial_z(\overline{u'w'}), \tag{5.11}$$

i.e. a slowly varying mean flow in the x-direction driven by waves in the x–z-plane. Again, we see a strong analogy between (5.10) and (5.11). Holton & Lindzen (1972) and Plumb (1977) were able to 'parametrise' the wave momentum flux as

$$(\overline{u'w'}) \sim \exp\left(-s\int_0^z \frac{N\mu}{k(\bar{u} - c)^2}\,\mathrm{d}z'\right), \tag{5.12}$$

where s is the sign of the z-component of the group velocity, k is the wavenumber in the x-direction and $c = \omega/k$ is the phase velocity, where ω is the wave frequency. In analogy, we can write for the inertial wave case,

$$(\overline{v'w'}) \sim \exp\left(-s\int_0^z \frac{2\Omega\zeta}{l(\bar{v} - c)^2}\,\mathrm{d}z'\right). \tag{5.13}$$

Considering two waves propagating towards the positive and negative y-direction, as proposed in § 4, the mean flow align can be written in the universal non-dimensional form,

$$\partial_t \hat{\bar{v}} + Re^{-1}\hat{\bar{v}} = -\frac{\partial}{\partial\hat{z}}\left(\exp\left(-\int_0^{\hat{z}} \frac{1}{\tilde{l}(\hat{\bar{v}} - 1)^2}\,\mathrm{d}\hat{z}'\right) - \exp\left(-\int_0^{\hat{z}} \frac{1}{\tilde{l}(\hat{\bar{v}} + 1)^2}\,\mathrm{d}\hat{z}'\right)\right), \tag{5.14}$$

where $Re^{-1} = \varsigma/\Omega_Q$, comparing the damping frequency with the QBO-like frequency Ω_Q. Note that for the internal gravity wave forcing, Renaud & Venaille (2020) scaled the Reynolds number as $Re^{-1} = \omega^2 h^2/(2\nu\gamma)$, where ω and h is the wave's frequency

https://doi.org/10.1017/jfm.2026.11559 Published online by Cambridge University Press

and amplitude,and ν and γ the kinematic viscosity and the buoyancy damping constant, respectively. In contrast to the classical QBO case, as previously mentioned, the waves in the SRI case are not forced by topography but by a flow instability. Thus, the wave amplitude depends on flow parameters like the damping constant and the angular velocity of the inner cylinder, and is also controlled by a nonlinear saturation of the growing waves, making it more difficult to estimate and include its value in the model. To bring (5.10) in the non-dimensional form (5.14), we then used the scaling $\hat{t} = \Omega_Q t$, $\hat{\bar{v}} = \bar{v}/c$, $\hat{z} = z\Omega_Q/c$, $\hat{w}' = \epsilon w'/c$, $\hat{v}' = \epsilon v'/c$, and for the axial wavenumber $\hat{l} = lc/(2\varsigma)$ and $\tilde{l} = \hat{l}\Omega_q/\Omega$. Here, c is the typical wave phase speed in the axial y-direction. Note that these scalings lead to a formal similarity between (5.14) and (37) of Renaud & Venaille (2020). However, we highlight that, in the SRI context, the Reynolds number $Re = \Omega_Q/\varsigma$ cannot be directly treated as an externally controlled parameter spanning from 0 to infinity, as in the Holton–Lindzen–Plumb framework of Renaud & Venaille (2020). In SRI experiments, Re is a non-trivial function that depends on other control parameters, such as the angular frequency of the modulations Ω_Q and friction ς. As a result, these parameters also influence the wave amplitude in a non-trivial way. In the regimes explored here, increasing Re (interpreted as the forcing parameter in Plumb's model) does not lead to a quasi-periodic route to chaos, as observed by Renaud & Venaille (2020), but may instead promote flow stabilisation, as described by Rüdiger *et al.* (2017) and Meletti *et al.* (2020).

To give an impression of the range of the non-dimensional parameters, we can use dimensional values from the numerical simulations. The mean velocity is, depending on the z-position, $\bar{v} \lessapprox 2 \times 10^{-3}$ m s^{-1}, $(\omega, \Omega, \Omega_Q) \approx (2 \times 10^{-1}, 4 \times 10^{-1}, 2 \times 10^{-3})$ rad s^{-1}, and the wavelength is $\lambda \approx 0.14$ m implying $l \approx 45$ rad m^{-1}, which gives an axial wave phase speed of $c \approx 4.4 \times 10^{-3}$ ms^{-1}. The solution of the non-dimensional version of (5.14) is controlled by Re^{-1} and $\tilde{l}$, where the former determines the flow regime (stable or oscillatory) and the amplitude, and the latter controls the period of the oscillations. We used a damping rate close to the angular frequency of the slow oscillations $\varsigma = 2\Omega_Q$ to be in the oscillatory regime. With the values above, $\tilde{l}$ is of order 1.

Note that using (5.14) but with only a single-wave forcing on the right-hand side, the mean flow would converge to a steady state with a narrow boundary layer at the inner cylinder wall and a constant flow above this layer. Adding a second wave, the mean flow becomes unstable and starts to oscillate. More details can be found from Holton & Lindzen (1972), Plumb (1977) and Renaud & Venaille (2020). Note that the mechanism described here has been reproduced in a laboratory experiment with internal gravity waves by Plumb & McEwan (1978). For a recent review, see also Semin & Pétrelis (2024).

Assuming wave forcing at $z = 0$, we solved (5.14) numerically using the fourth-order Runge–Kutta scheme for the time derivative and the trapezoidal rule for the integrals. To connect (5.14) more tightly to the simulation, we used the simulated axial mean flow profile $\overline{\langle u_z \rangle_z}^t$ as an initial condition. The profile considered is the one shown in figure 11(a) as the blue solid line. We further show the momentum flux taken from the SRI simulation in figure 11(b). The slopes of the curves shown give the forcing of the low-frequency oscillations. We see that at the inner part of the gap (left-hand side in figures 11a and 11b), the sign of the forcing, with positive/negative slope, differs from that at the outer part, with negative/positive slopes. For (5.14) of the QBO-like model, the sign differs between a region $0 \lessapprox z \lessapprox 0.1 \cdot \max(z)$ and $z \gtrapprox 0.1 \cdot \max(z)$. This leads to a downward propagation of the QBO-like signal and usually different flow directions close to the bottom and further up (see, e.g. figure 3a of Renaud & Venaille (2020)).

https://doi.org/10.1017/jfm.2026.11559 Published online by Cambridge University Press

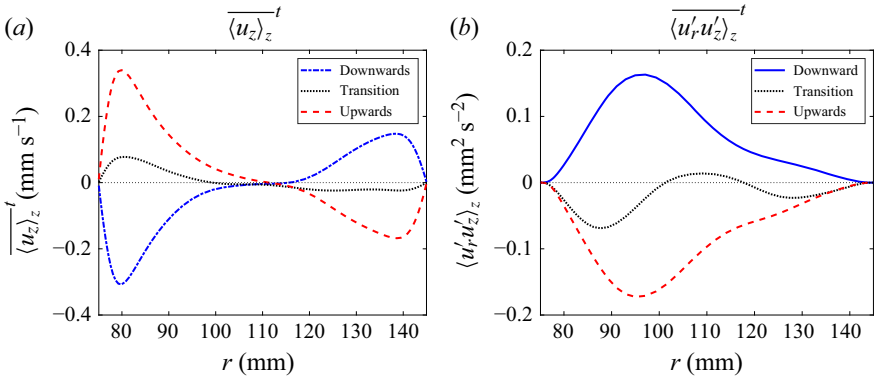


Figure 11. (*a*) Radial distribution of the axial velocity averaged in the axial direction and in time ($\overline{\langle u_z\rangle_z}^t$) at $(r, \phi) = (r_{in} + d/3, 0)$ considering three different time intervals: when the spiral is travelling upwards, downwards and during the transition. (*b*) Axial and time mean of the eddy momentum flux ($\overline{\langle u_r'u_z'\rangle_z}^t$).

The result of the integration is shown in figure 12(*a*), where we plotted the axial velocity $\overline{v}(t, z)$ (corresponding to $= \langle u_z\rangle_z(t, r)$ in the DNS) for $Re^{-1} = 2$ and $\tilde{l} = 1$. It can be seen that over the entire period considered, the axial flow direction oscillates. The largest amplitudes can be found moving towards $z = 0$ in the coordinate system presented in figure 10, which corresponds to the area near $r = r_{in}$ in the DNS results. The amplitude weakens away from the inner boundary. Comparing the mean flow and the wave forcing of the QBO model (not shown) with the corresponding time-series of the SRI simulations shown in figure 4, we find qualitative agreements concerning the shape and the phase lag of the curves. This suggests that the mechanism we describe here using the simple QBO model is consistent with the data shown in figure 4 where we found a correlation between $\partial_r\langle u_z'u_r'\rangle_z$ and $\langle u_z\rangle_z$, corresponding to $\partial_z(\overline{v'w'})$ and $\bar{v}$ of the QBO model. We hence conclude that the wave–mean flow interaction of the QBO model is also a relevant process for the oscillating axial mean flow in the SRI simulation.

5.4. *Comparison of the SRI data with the QBO-like model*

A limitation of the model sketched is the neglect of the radially bounded nature of our SRI system, where waves near the inner and outer boundaries strongly influence the flow. This effect is clear when we compare the t–r-Hovmöller diagrams of the QBO-like model in figure 12(*a*) with the low-frequency modulations of u_z shown for the SRI simulation in figure 12(*b*). The modulation amplitude is large at both radial boundaries since both are source regions for waves. A first step to adapt (5.14) to the SRI simulation is to solve it for a wave source at $z = 0$ and at $z = 1$, and then superpose both solutions. For the SRI, the waves at the inner and outer boundary are phase shifted, as can be seen, e.g. in figure 6 of Yavneh *et al.* (2001) or figure 2 of Molemaker *et al.* (2001). In fact, for an instability due to wave resonance, a phase shift between the resonating waves is rather typical. Hence, we applied a 53° phase shift to the waves at $z = 1$. Note that we applied the phase shift heuristically, lacking a theory for the consequences of this shift to the low-frequency oscillations. It is, however, empirically motivated by SRI data, where there is a phase shift between the wave patterns near the inner and outer cylinders. Thus, in this framework, we do not solve the aligns at the outer boundary; instead, we simply mirror the inner-cylinder solution to the outer wall and heuristically apply a phase shift, which is then added linearly to the QBO-like solution (presented in figure 12*a*) to obtain a qualitative

https://doi.org/10.1017/jfm.2026.11559 Published online by Cambridge University Press

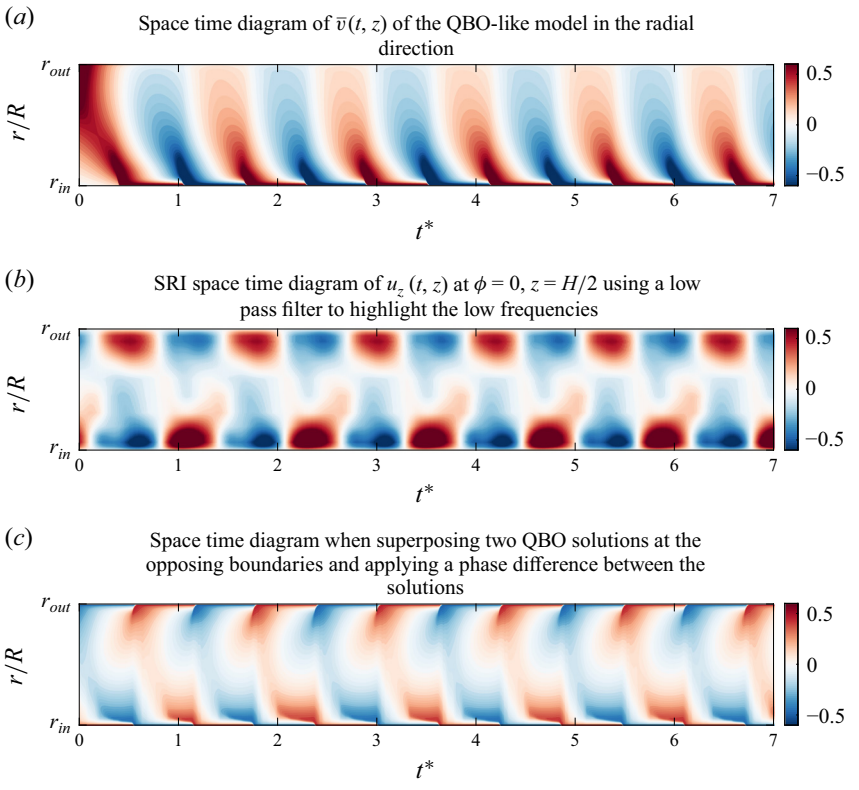


Figure 12. Comparison of space–time diagrams using a non-dimensional time*. The time is normalised for better comparison, such that the modulations of the QBO model and the DNS are the same. (*a*) QBO model; (*b*) SRI axial velocity u_z modulations at mid-height position $z = H/2$; (*c*) QBO-like model considering two boundaries by mirroring the results of panel (*a*) at the top and phase shifting them 53°. By considering two boundaries, the results of the QBO-like model align more closely with the low-pass-filtered SRI data shown in panel (*b*). (*a*) Space–time diagram of $\overline{v}(t, z)$ of the QBO-like model in the radial direction, (*b*) SRI space–time diagram of $u_z(t, r)$ at $\phi = 0$, $z = H/2$ using a low pass filter to highlight the low frequencies, (*c*) Space–time diagram when superposing two QBO solutions at the opposing boundaries and applying a phase difference between the solutions.

representation of the outer cylinder's contribution. The result of superposing the forcing at both boundaries and applying a phase shift is shown in figure 12(*c*), where the space–time structure of the modified QBO model becomes more consistent with the bounded SRI results. Despite these limitations, the general features of figures 12(*b*) and 12(*c*) are not very different: both systems display QBO-like oscillations, and in both cases, boundary influences extend only until a finite distance from the boundaries.

Finally, in figure 13, we show a comparison of a time series of a mirrored QBO-like result similar to figure 12(*c*) with the corresponding SRI time series. Here, the comparison is done in dimensional units using $Re^{-1} = 2$ and $\tilde{l} = 1.35$. The time series is taken both at mid-gap ($r = r_{in} + d/2$) and, for the DNS, at mid-height position ($z = H/2$). In dimensional units, the agreement between the time series is very good, although the frequency of the QBO-like model is somewhat slightly higher.

In summary, we note that the real SRI configuration, as captured by DNS, is naturally more complex than the one modelled with the reduced QBO-like model. A quantitative analysis of the SRI wave–mean flow interactions would require an appropriately

https://doi.org/10.1017/jfm.2026.11559 Published online by Cambridge University Press

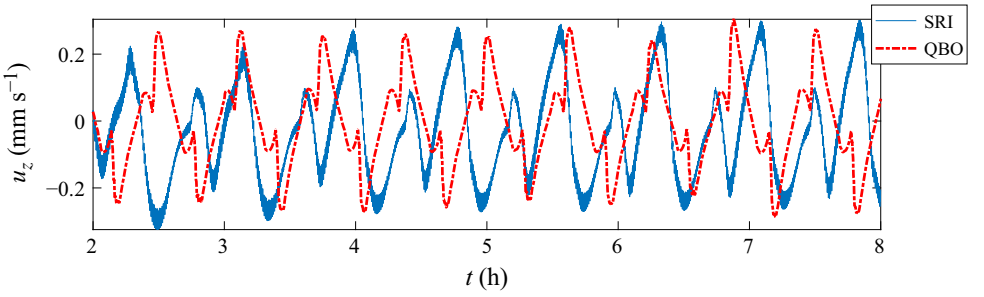


Figure 13. Comparison of dimensional time series between the mirrored QBO-like model (5.14) and the SRI axial velocity averaged in the azimuthal direction $\langle u_z \rangle_\phi$. The time series have been taken at mid-gap ($r = r_{in} + d/2$) position and the SRI time series also at mid-height position ($z = H/2$). For the simulation, we used $Re^{-1} = 2$ and $\tilde{l} = 1.35$. The scaling is given in the text.

formulated numerical model, starting from (2.2). Therefore, we do not attempt to justify the realism of the inertial wave–mean flow model in modelling the SRI spiral pattern changes. Rather, we use this simplified model to show how it produces similar results that support an interpretation of the spiral propagation changes in the axial direction with QBO-like features, illustrating how the low-frequency oscillations in the SRI can be interpreted as resulting from mean-flow/instability interactions.

6. Conclusions

This study explores the interactions between axial modes and spiral components in a stratified, rotating flow that develops strato-rotational instability (SRI). The findings demonstrate that the SRI engenders complex oscillatory dynamics, previously observed by Meletti *et al.* (2020), significantly alter the mean flow. The oscillations are characterised by the selective activation of distinct axial wavenumbers, corresponding to upward and downward propagating spiral modes that alternate in dominance.

The application of Radon transform (RT) enabled a clear separation of the upward and downward spiral components, revealing their interaction with the mean flow. This interaction manifests as amplitude modulations, which have been robustly captured in both numerical simulations and experimental data (Meletti *et al.* 2020, 2023; Riedinger *et al.* 2010; Lopez & Marques 2022). We observed here the presence of out-of-phase modulated harmonic waves associated with specific azimuthal wavenumbers, further indicating that the dynamics are governed by nonlinear wave–mean flow interactions. Inspired by these RT findings, a simplified toy model was developed to interpret the physics underlying the spiral pattern changes associated with amplitude modulations. This model proposes that the observed phenomena can be interpreted as two individual wave-like spirals propagating in opposite directions along the axial axis, added in a simple linear superposition. The RT findings also suggested that these spirals should be individually modulated and that these modulations should be out of phase. This was incorporated into the toy model. By linearly superimposing these two modulated wave-like travelling spirals, the toy model successfully reproduced the observed spiral pattern changes, providing an interpretation of the underlying physics observed.

However, the important question of the origin of the individual modulation of each spiral still had to be addressed. The observed base flow/instability interaction, indicated by changes in the mean flow, inspired the comparison of the individual modulations to a quasi-biennial oscillation (QBO)-like phenomenon. To model this, we employed a simplified linearised QBO-like dynamics approach, following the models proposed by

https://doi.org/10.1017/jfm.2026.11559 Published online by Cambridge University Press

Holton & Lindzen (1972), Plumb (1977), Seelig & Harlander (2015) and Renaud & Venaille (2020) to derive a QBO-like model in the axial direction, explaining the mean-flow/instability mechanisms. This model successfully replicates the qualitative features observed in the axial velocity, confirming that the QBO-like behaviour that arises from the mean-flow/instability interaction can explain the individual spiral modulations previously introduced in the wave-like toy-model.

Finally, we note that the QBO-like framework developed here may also provide inspiration for interpreting other reversal phenomena observed in stratified fluids. In particular, QBO-like reversals have been reported in penetrative convection systems, where a convective layer is attached to a stably stratified region and drives the emission of internal waves (Couston *et al.* 2018; Lecoanet *et al.* 2019). In these cases, large-scale circulations arise as a byproduct of a base-flow instability interaction, and mean-flow reversals can emerge. Although the physical configurations differ from the present study, this conceptual similarity suggests that related wave–mean flow interaction processes may be at play. Furthermore, the reversal phenomenon reported by Couston *et al.* (2018) was obtained numerically and, to the best of our knowledge, has not yet been confirmed experimentally. One proposed explanation for this discrepancy was the relatively high Prandtl number used in laboratory experiments (typically water), compared with the lower Prandtl numbers considered in numerical studies. However, more recent experimental investigations using gas (Dorel *et al.* 2023) have not yet provided clear confirmation of the predicted reversals. It would therefore be interesting to explore whether a similar QBO-like synchronisation mechanism operating in our system could help clarify the conditions under which reversals emerge or are suppressed in penetrative convection systems. Beyond this analogy, our results may also connect to work related to synchronisation phenomena in QBO-like systems (e.g. Read & Castrejón-Pita 2010). Recent studies have shown that when multiple wave forcings coexist, their nonlinear interaction with the mean flow can promote or suppress periodic behaviour depending on propagation and damping characteristics (Chartrand, Nadeau & Venaille 2024). In contrast to these studies, where multiple standing waves are imposed at the same boundary, our configuration introduces the possibility of synchronisation between QBO-like oscillations driven by standing waves originating from different boundaries.

Acknowledgements. The authors thank A. Krebs, T. Seelig, Arantxa Alonso, Francisco Marques, Isabel Mercader, Oriol Batiste, Á lvaro Meseguer, A. Randriamampianina and I. Raspo for the discussions and support. We also thank the researchers from the Nonlinear Fluid Dynamics of the Universitat Politècnica de Catalunya for the constructive discussions. We finally thank the anonymous reviewers for their comments that helped us improve the clarity of this paper.

Funding. U.H. acknowledges support from the DAAD project 'Combined studies of baroclinic waves with methods of data assimilation' (57560889). G.M. acknowledges the financial support from the DFG core facility center 'Physics of rotating fluids', DFG HA 2932/10-1. G.M. and J.C. acknowledge support from the Agencia Estatal de Investigación through the grant CNS2023-144360 funded by the 'European Union NextGenerationEU/PRTR' and the grant PID2024-159949NA-I00. J.C. also thanks the Severo Ochoa and María de Maeztu Program for Centers and Units of Excellence in R&D (CEX2020-001084-M) and the Fundación Ramón Areces. This work has been supported by the French government, through the UCAJEDI Investments in the Future project managed by the National Research Agency (ANR) with the reference number ANR-15-IDEX-01.

Declaration of interests. The authors report no conflict of interest.

https://doi.org/10.1017/jfm.2026.11559 Published online by Cambridge University Press

Appendix A. Radon transform

The Radon transform $R(r, \phi)$ consists of a Fourier-like technique developed by Radon (1917). This technique transforms a function defined on a given plane $\eta(z, t)$ into a line domain. These lines are inside the original 2-D space, with the values of a particular line being equal to the line integral of the original function (over that projected line). Therefore, the Radon transform consists on an angular projection given by

$$R(r, \phi) = \iint \eta(z, t)\delta\left(z\cos\phi + t\sin\phi - r\right) \mathrm{d}z\mathrm{d}t, \tag{A1}$$

where δ the Dirac delta function. Here, $r = z\cos\phi + z\sin\phi$ and ϕ are respectively the radius and angle, in polar coordinates, that define the line where the 2-D space will be projected. Furthermore, ϕ can vary from 0 to π. The use of the Dirac delta function forces the integration of $\eta(x, t)$ along the line on which the plane will be projected. If we consider a two-dimensional spatiotemporal wave signal $\eta(z, t)$, travelling in the z direction, the angle ϕ can be converted into a wave drift velocity c through the transformation (Almar *et al.* 2014)

$$c = \tan(\phi)\frac{\mathrm{d}z}{\mathrm{d}t}, \tag{A2}$$

where $\mathrm{d}z$ and $\mathrm{d}t$ are respectively the spatial and temporal resolution. If the $\eta(z, t)$ signal contains multiple waves, multiple local peaks (r,ϕ) will appear in the Radon spectra. Each propagating crest in the spatiotemporal $\eta(z, t)$ field is detected from their signatures in the Radon space corresponding to a peak value, where the ϕ angle indicates the direction of propagation with respect to the z spatial direction considered. The phase speed of a wave propagating it the z direction will then be obtained using (A2). In the case of a spatiotemporal wave field containing incoming (η_{up}) and outgoing (η_{down}) waves, such that $\eta(z, t) = \eta_{up}(z, t) + \eta_{down}(z, t)$, each component can be separated using the inverse RT. The inverse RT is a back-projection of $R(r, \phi)$ at given angles ϕ. The total initial wave signal $\eta(z, t)$ can be reconstructed from the Radon space to the physical space as (Almar *et al.* 2014)

$$\eta = \iint R(r, \phi)\, \mathrm{d}\phi\mathrm{d}r, \tag{A3}$$

therefore, the separated wave components can be obtained by applying the limits of integration to the inverse Radon transform as

$$\begin{aligned} \eta_{up}(z, t) &= \int_{-\infty}^{+\infty}\int_{1}^{89} R(r, \phi)\, \mathrm{d}\phi\mathrm{d}r, \\ \eta_{up}(z, t) &= \int_{-\infty}^{+\infty}\int_{91}^{179} R(r, \phi)\, \mathrm{d}\phi\mathrm{d}r. \end{aligned} \tag{A4}$$

Note that the Radon transforms have been successfully applied for separating wave components in different fields, from a surface or internal ocean wave dynamics, to pressure fluctuation concerning aeroacoustic applications (Copeland, Ravichandran & Trivedi 1995; Challenor, Cipollini & Cromwell 2001; Zhang, Zhang & Qi 2009; Yoo *et al.* 2011; Martarelli, Castellini & Tomasini 2013; Almar *et al.* 2014).

https://doi.org/10.1017/jfm.2026.11559 Published online by Cambridge University Press

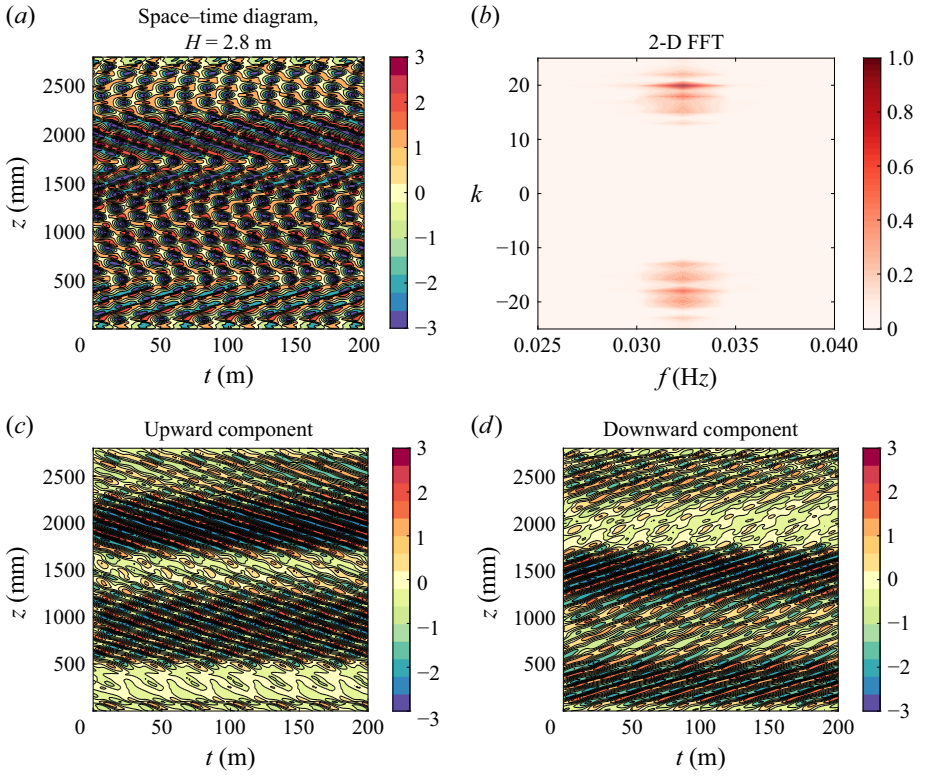


Figure 14. Separation of upward and downward axial travelling components space–time diagram using the Radon transform. Results are of u_ϕ numerical simulations with $Re = 400$, $\mu = 0.35$, $\Delta T/\Delta z \approx 5.71$ Km^{-1} and cavity height of $H = 2800$ mm (four times larger than the previous one considered). (*a*) Space–time diagram showing the full spiral propagation, $H = 2.8$ m; (*b*) 2-D-FFT of the full spiral; (*c*) space–time diagram of the spiral component travelling upward; (*d*) space–time diagram of the spiral component travelling downward.

Appendix B. Geometry variations

The RT was also used to separate the upward and downward travelling spirals in the more complicated patterns observed in a cavity four times larger than the previous set-up considered (which was based on the experimental cavity presented by Seelig *et al.* (2018) and Meletti *et al.* (2020)), i.e. instead of an $H = 700$ mm height cavity, we consider a $H = 2800$ mm tall cavity.

In figure 14, the separation of the more complicated patterns in the $H = 2800$ mm cavity also leads to two spirals with similar wavelengths travelling in opposite axial directions, with the final spiral pattern formed by a linear superposition of these two separated components. We highlight that the separation of the spiral components using u_ϕ and $u'_\phi = u_\phi - \overline{u_\phi}$ are equivalent since the base flow propagates in the azimuth direction; therefore, it is filtered out by the RT in the axial direction. From figure 14, it becomes clear that the changes in the final spiral direction are associated with the amplitude of each separated axial spiral component since the spiral amplitudes are enhanced in different regions of the axial axis. Note that, when the amplitudes in the upward travelling component are enhanced, the amplitude in the downward component becomes smaller and the opposite is also true, maintaining constant the energy contained in both amplitudes, with $A_1 + A_2 = constant$. Adding the upward (figure 14*c*) and downward (figure 14*d*) spiral components, the initial spiral pattern in figure 14(*a*) is reconstructed, showing

https://doi.org/10.1017/jfm.2026.11559 Published online by Cambridge University Press

that the spiral patterns arise from the linear superposition of these two upward and downward spiral components with different wave numbers, travelling in time with the same frequencies ω (in Hz in the x-axis of figure 14*b*).

The impact of the outer cylinder wall on SRI development was also investigated. In our numerical simulations, the inner cylinder radius $r_{in} = 75$ mm was kept constant, while the outer radius r_{out} was increased ($r_{out} > 145$ mm), with all other parameters remaining unchanged. Suppression of the SRI was observed when the outer cylinder radius reached $r_{out} = 180$ mm, with only small oscillations occurring at the very beginning of the simulations, which soon vanished into a stable flow with no further development of SRI oscillations after more than 3 hours (in physical time) of simulation.

Although increasing the external radius to $r_{out} \geqslant 180$ mm led to stable SRI flows, when the stratification was increased from $\Delta T/\Delta z = 5.71$ K m^{-1} to $\Delta T/\Delta z = 11.43$ K m^{-1}, SRI oscillations were again observed. These results differ from those observed by Rüdiger & Shalybkov (2009), who related to the linear analysis of the SRI, where a wider gap required rather weak stratification to support the SRI, but, in our case, we are changing the aspect ratio of the cavity when we increase the gap size while keeping the height constant. However, they agree with their results considering variations in the Froude number leading to a stable SRI solution. Moreover, we note that changes in r_{out} led to a delay in the instability development. It is also important to note that the evaluation presented here accounts for the influence of nonlinearities in the simulations, which differs from Rüdiger & Shalybkov (2009). Simulations with a slightly increased gap size, from $d = 70$ mm to $d = 95$ mm, developed the SRI only after $t > 50$ min. When $d = 105$ mm and $\Delta T/\Delta z = 11.43$ K m^{-1}, the time necessary for the first SRI oscillations increased to $t > 100$ min. Therefore, it is not possible to conclusively say from these investigations whether the instability is suppressed in larger gap sizes (or without an external wall) or if it will simply develop at a later time. When the outer cylinder wall was increased to $r_{out} = 290$ mm while maintaining the higher $\Delta T/\Delta z = 11.43$ K m^{-1}, the SRI oscillations were once again suppressed. Thus, while it is not possible to conclusively determine from this simple qualitative investigation whether the SRI will no longer occur in larger gap widths or if its development is merely delayed, it is clear that the presence of the outer wall can influence the timing of SRI development. A more comprehensive study of the SRI parameters would be important to gain a better understanding of the influence of the outer cylinder wall and critical layers on the development of these instabilities, but our data suggested that critical layers play a significant role in SRI circulation dynamics, which should be further explored in future studies.

References

Abide, S., Binous, M.S. & Zeghmati, B. 2017 An efficient parallel high-order compact scheme for the 3D incompressible Navier–Stokes aligns. *Intl J. Comput. Fluid Dyn.* **31** (4–5), 214–229.

Abide, S. & Viazzo, S. 2005 A. 2D compact fourth-order projection decomposition method. *J. Comput. Phys.* **206** (1), 252–276.

Abide, S., Viazzo, S., Raspo, I. & Randriamampianina, A. 2018 Higher-order compact scheme for high-performance computing of stratified rotating flows. *Comput. Fluids* **174**, 300–310.

Almar, R., Michallet, H., Cienfuegos, R., Bonneton, P., Tissier, M. & Ruessink, G. 2014 On the use of the Radon transform in studying nearshore wave dynamics. *Coast. Engng* **92**, 24–30.

Boubnov, B.M., Gledzer, E.B. & Hopfinger, E.J. 1995 Stratified circular Couette flow: instability and flow regimes. *J. Fluid Mech.* **292**, 333–358.

Challenor, P.G., Cipollini, P. & Cromwell, D. 2001 Use of the 3D Radon transform to examine the properties of oceanic Rossby waves. *J. Atmos. Ocean. Tech.* **18** (9), 1558–1566.

Chartrand, X., Nadeau, L.-P. & Venaille, A. 2024 Recovering quasi-biennial oscillations from chaos. *J. Atmos. Sci.* **81** (7), 1213–1224.

https://doi.org/10.1017/jfm.2026.11559 Published online by Cambridge University Press

COPELAND, A.C., RAVICHANDRAN, G. & TRIVEDI, M.M. 1995 Localized Radon transform-based detection of ship wakes in SAR images. *IEEE Trans. Geosci. Remote* **33** (1), 35–45.

COUSTON, L.-A., LECOANET, D., FAVIER, B., BARS, L. & Michael 2018 Order out of chaos: slowly reversing mean flows emerge from turbulently generated internal waves. *Phys. Rev. Lett.* **120** (24), 244505.

DOREL, V., LE GAL, P., LE BARS, M. 2023 Experimental study of the penetrative convection in gases. *Phys. Rev. Fluids* **8** (10), 103501.

DUBRULLE, B., MARIÉ, L., NORMAND, C.H., RICHARD, D., HERSANT, F. & ZAHN, J.-P. 2004 An hydrodynamic shear instability in stratified disks. *Astron. Astrophys.* **429**, 1–13.

FLÓR, J.B., HIRSCHBERG, L., OOSTENRIJK, B.-H. & VAN HEIJST, G.J.F. 2018 Onset of centrifugal instability at a rotating cylinder in a stratified fluid. *Phys. Fluids* **30** (8), 084103.

FROMANG, S. & LESUR, G. 2019 Angular momentum transport in accretion disks: a hydrodynamical perspective. *Eas Publ.* **82**, 391–413.

HARLANDER, U., SCHÖNFELDT, H.-J. & METZ, W. 2000 Rossby waveguides in high-latitude shear flows with boundaries. *J. Geophys. Res.: Oceans* **105** (C7), 17063–17078.

HOLTON, J.R. & LINDZEN, R.S. 1972 An updated theory for the quasi-biennial cycle of the tropical stratosphere. *J. Atmos. Sci.* **29** (6), 1076–1080.

HOSKINS, B.J. & AMBRIZZI, T. 1993 Rossby wave propagation on a realistic longitudinally varying flow. *J. Atmos. Sci.* **50**, 1661–1671.

HUGUES, S. & RANDRIAMAMPIANINA, A. 1998 An improved projection scheme applied to pseudospectral methods for the incompressible Navier–Stokes aligns. *Intl J. Numer. Meth. Fluids* **28** (3), 501–521.

LE BARS, M. & LE GAL, P. 2007 Experimental analysis of the stratorotational instability in a cylindrical Couette flow. *Phys. Rev. Lett.* **99** (6), 064502.

LE DIZÈS, S. & BILLANT, P. 2009 Radiative instability in stratified vortices. *Phys. Fluids* **21** (9), 096602.

LE DIZÈS, S. & RIEDINGER, X. 2010 The strato-rotational instability of Taylor–Couette and Keplerian flows. *J. Fluid Mech.* **660**, 147–161.

LECOANET, D., CANTIELLO, M., QUATAERT, E., COUSTON, L.-A., BURNS, K.J., POPE, B.J.S., JERMYN, A.S., FAVIER, B. & LE BARS, M. 2019 Low-frequency variability in massive stars: core generation or surface phenomenon? *Astrophys. J. Lett.* **886** (1), L15.

LINDZEN, R.S. & HOLTON, J.R. 1968 A theory of the quasi-biennial oscillation. *J. Atmos. Sci.* **25** (6), 1095–1107.

LOPEZ, J.M. & MARQUES, F. 2020 Impact of centrifugal buoyancy on strato-rotational instability. *J. Fluid Mech.* **890**), A9.

LOPEZ, J.M. & MARQUES, F. 2022 Stratified Taylor–Couette flow: nonlinear dynamics. *J. Fluid Mech.* **930**, A2.

LYRA, W. & UMURHAN, O.M. 2019 The initial conditions for planet formation: turbulence driven by hydrodynamical instabilities in disks around young stars. *Publ. Astron. Soc. Pac.* **131** (1001), 072001.

MARTARELLI, M., CASTELLINI, P. & TOMASINI, E.P. 2013 Subsonic jet pressure fluctuation characterization by tomographic laser interferometry. *Exp. Fluids* **54** (12), 1626.

MELETTI, G., ABIDE, S., VIAZZO, S. & HARLANDER, U. 2023 A parameter study of strato-rotational low-frequency modulations: impacts on momentum transfer and energy distribution. *Phil. Trans. R. Soc. A* **381** (2246), 20220297.

MELETTI, G., ABIDE, S., VIAZZO, S., KREBS, A. & HARLANDER, U. 2020 Experiments and long-term high-performance computations on amplitude modulations of Strato-Rotational flows. *Geophys. Astrophys Fluid Dyn.* 1–25.

MOLEMAKER, M.J., MCWILLIAMS, J.C. & YAVNEH, I. 2001 Instability and equilibration of centrifugally stable stratified Taylor–couette flow. *Phys. Rev. Lett.* **86** (23), 5270.

PARK, J. 2012 Waves and instabilities on vortices in stratified and rotating fluids. PhD thesis, Ecole Polytechnique X.

PARK, J. & BILLANT, P. 2013 The stably stratified Taylor–Couette flow is always unstable except for solid-body rotation. *J. Fluid Mech.* **725**, 262–280.

PEDLOSKY, J. 1987 *Geophysical Fluid Dynamics*. Springer-Verlag.

PLUMB, R.A. 1977 The interaction of two internal waves with the mean flow: implications for the theory of the quasi-biennial oscillation. *J. Atmos. Sci.* **34** (12), 1847–1858.

PLUMB, R.A. & MCEWAN, A.D. 1978 The instability of a forced standing wave in viscous stratified fluid: a laboratory analogue of the Quasi-Biennial Oscillation. *J. Atmos. Sci.* **35**, 1827–1839.

RADON, J. 1917 Über die bestimmung von funktionen durch ihre intergralwerte längs gewisser. In *Reports on the Proceedings of the Saxony Academy of Science*, pp. 262–277.

https://doi.org/10.1017/jfm.2026.11559 Published online by Cambridge University Press

READ, P.L. & CASTREJÓN-PITA, A.A. 2010 Synchronization in climate dynamics and other extended systems. In *Nonlinear Dynamics and Chaos: Advances and Perspectives* (ed. M. Thiel, J. Kurths, M. Romano, G. Károlyi & A. Moura), Understanding Complex Systems, pp. 153–176. Springer.

RENAUD, A. & VENAILLE, A. 2020 On the Holton–Lindzen–Plumb model for mean flow reversals in stratified fluids. *Q. J. R. Meteorol. Soc.* **146** (732), 2981–2997.

RIEDINGER, X., MEUNIER, P. & LE DIZÈS, S. 2010 Instability of a vertical columnar vortex in a stratified fluid. *Exp. Fluids* **49** (3), 673–681.

RÜDIGER, G., SEELIG, T., SCHULTZ, M., GELLERT, M., EGBERS, C. & HARLANDER, U. 2017 The stratorotational instability of Taylor–Couette flows of moderate Reynolds numbers. *Geophys. Astrophys. Fluid Dyn.* **111** (6), 429–447.

RÜDIGER, G. & SHALYBKOV, D.A. 2009 Stratorotational instability in MHD Taylor–Couette flows. *Astron. Astrophys.* **493**, 375–383.

SEELIG, T. & HARLANDER, U. 2015 Can zonally symmetric inertial waves drive an oscillating zonal mean flow? *Geophys. Astrophys. Fluid Dyn.* **109** (6), 541–566.

SEELIG, T., HARLANDER, U. & GELLERT, M. 2018 Experimental investigation of stratorotational instability using a thermally stratified system: instability, waves and associated momentum flux. *Geophys. Astrophys. Fluid Dyn.* **112** (4), 239–264.

SEMIN, B. & PÉTRELIS, F. 2024 Quasi-biennial oscillation: laboratory experiments. *C. R. Phys.* **25** (S3), 1–25.

SHALYBKOV, D. & RÜDIGER, G. 2005 Stability of density-stratified viscous Taylor–Couette flows. *Astron. Astrophys.* **438** (2), 411–417.

VISSER, R. & DULLEMOND, C.P. 2010 Sub-Keplerian accretion onto circumstellar disks. *Astron. Astrophys.* **519**, A28.

WANG, C. & BALMFORTH, N.J. 2018 Strato-rotational instability without resonance. *J. Fluid Mech.* **846**, 815–833.

WITHJACK, E.M. & CHEN, C.F. 1974 An experimental study of Couette instability of stratified fluids. *J. Fluid Mech.* **66** (4), 725–737.

YAVNEH, I., MCWILLIAMS, J.C. & MOLEMAKER, M.J. 2001 Non-axisymmetric instability of centrifugally stable stratified Taylor–Couette flow. *J. Fluid Mech.* **448**, 1–21.

YOO, J., FRITZ, H.M., HAAS, K.A., WORK, P.A. & BARNES, C.F. 2011 Depth inversion in the surf zone with inclusion of wave nonlinearity using video-derived celerity. *J. Waterway Port Coastal, Ocean Engng* **137** (2), 95–106.

ZHANG, S., ZHANG, C. & QI, Z. 2009 Wave swash velocity estimation using ridgelet transform. In *2009 9th International Conference on Electronic Measurement & Instruments*, pp. 4–1078. IEEE.

https://doi.org/10.1017/jfm.2026.11559 Published online by Cambridge University Press